LA-UR-14-28164
Approved for public release; distribution is unlimited.

Title: (U) Equation of State and Compaction Modeling for CeO2

Author(s): Fredenburg, David A.
Chisolm, Eric D.

Intended for: Report

Issued: 2014-10-20

(U) Equation of State and Compaction Modeling for CeO_2

D.A. Fredenburg and E.D. Chisolm
Los Alamos National Laboratory, Los Alamos, NM 87545
dafreden@lanl.gov
LA-UR-14-XXXXXX

October 8, 2014

Abstract

Recent efforts have focused on developing a solid-liquid and three-phase equation of state (EOS) for CeO_2, while parallel experimental efforts have focused on obtaining high-fidelity Hugoniot measurements on CeO_2 in the porous state. The current work examines the robustness of two CeO_2 SESAME equations of state, a solid-liquid EOS, 96170, and a three-phase EOS, 96171, by validating the EOS against a suite of high-pressure shock compression experiments on initially porous CeO_2. At lower pressures compaction is considered by incorporating a two-term exponential form of the P-α compaction model, using three separate definitions for $\alpha(P)$. Simulations are executed spanning the partially compacted and fully compacted EOS regimes over the pressure range 0.5 - 109 GPa. Comparison of calculated Hugoniot results with those obtained experimentally indicate good agreement for all definitions of $\alpha(P)$ with both the solid-liquid and three-phase EOS in the low-pressure compaction regime. At higher pressures the three-phase EOS does a better job at predicting the measured Hugoniot response, though at the highest pressures EOS 96171 predicts a less compliant response than is observed experimentally. Measured material velocity profiles of the shock-wave after it has transmitted through the powder are also compared with those simulated using with solid-liquid and three-phase EOS. Profiles lend insight into limits of the current experimental design, as well as the threshold conditions for the shock-induced phase transition in CeO_2.

Contents

Executive Summary

One-dimensional simulations using either a solid-liquid or three-phase equation of state (EOS) were performed on a suite of high-strain-rate impact experiments on CeO_2 with an initial porous density of 4.03 g/cm^3. Results indicate that CeO_2 remains in the low-pressure cubic fluorite phase within the compaction regime and at pressures up to ∼12 GPa. As the magnitude of shock loading is increased, the three-phase EOS exhibits a stepped wave-structure at ∼24 GPa, indicating onset of the equilibrium shock-induced phase transition to the high-pressure orthorhombic phase. Late-time material velocity profiles recorded for the highest impact velocity experiments also display a characteristic stepped profile, and may reveal information regarding kinetics of a shock-assisted transformation and/or reaction.

Recent advancements in experimental techniques for characterizing the initial and final state of shock compressed porous materials have resulted in high-fidelity compaction and EOS measurements on initially porous CeO_2. Results are used for EOS and compaction model validation for calculations performed at impact velocities ranging from 0.14 to 5.6 km/s. Effects of mesh size, artificial viscosity, and "impedance matching" on the calculated Hugoniot state and transmitted wave profiles are examined explicitly.

Three distinct implementations of the P-α compaction model are employed on both the solid-liquid and three-phase equations of state to determine the effect of varying the definition of $\alpha(P)$ on the compaction and EOS response. Definitions for $\alpha(P)$ are based on the ambient crystal density and the solid and porous Hugoniots. For pressures less than ∼5 GPa (resulting in compression of the initially porous CeO_2 to approximately 90% of the crystal density) there is very little difference observed between the three $\alpha(P)$ implementations. However, as pressures approach those required to reach the solid calculations diverge, with the definition for $\alpha(P)$ based on the ambient crystal density showing the best agreement with experimental results. Comparison of experimental data with calculations from both the solid-liquid and three-phase EOS also indicate that CeO_2 retains its initial cubic fluorite structure throughout the compaction process.

As pressure reaches ∼24 GPa for calculations performed with the solid-liquid EOS, Hugoniot results from the three $\alpha(P)$ definitions converge and asymptote to a linear P-V response with increasing pressure. A vertical P-V response is not achieved in the experiments until ∼52 GPa, and consequently the calculated response deviates substantially from experiment at these high pressures. Implementation of the three-phase EOS shows better agreement at elevated pressures, indicating the material likely undergoes a shock-induced phase transition from cubic fluorite to orthorhombic. However, for the three-phase EOS the definitions for $\alpha(P)$ do not converge to a similar response, and varying levels of agreement are observed between the calculated and experimental Hugoniots at high pressures. At the highest pressures investigated, ∼1.1 Mbar, $\alpha(P)$ based on the porous Hugoniot comes the closest to matching experimental results.

Profiles of the shock wave after it had transmitted through the powder compact were recorded in the experiments, and comparison was made with those produced from simulations. Calculated results indicate that the specific definition for $\alpha(P)$ has little effect on the propagated wave shape for all experiments whose impact velocities exceed ∼0.4 km/s. Furthermore, for impact velocities less than ∼0.4 km/s release and edge waves in the experiments interact with the propagating wave in the bulk of the powder such that the shock wave is in a non-steady state prior to reaching the powder/window interface. As a consequence, a redesign of the experimental fixture is required to obtain true Hugoniot data in this low velocity regime.

Wave profiles also lend insight into the threshold pressure for phase transition. At ∼24 GPa wave profiles calculated with the three-phase EOS exhibit a stepped structure, where evidence of this type of structure is not observed in either the solid-liquid EOS or at higher pressures with the three-phase EOS. This indicates that at ∼24 GPa the three-phase EOS predicts CeO_2 is on the cusp of the equilibrium phase transition from cubic to orthorhombic. Interestingly, ∼24 GPa is also where the P-V results calculated with the three-phase EOS begin to oscillate around a nearly vertical response, suggesting that as pressures are increased thermal effects become more important and can serve to counter the compressive loads. With the vertical response not observed in experiments until 52 GPa, it may be that an additional transformation mechanism is responsible for the increased compression observed experimentally in the 24 - 52 GPa pressure range. However, neither the present calculations or experiments can support this hypothesis.

Another interesting feature characteristic of the measured wave profiles for the three highest pressure experiments is a steplike structure recorded at late times. While similar in form to that observed computationally at ∼24 GPa for simulations performed with the three-phase EOS, this step is observed over a broad pressure range and occurs toward the end of the flat-top region, not toward the beginning as indicated in the ∼24 GPa calculation. The origin of this high-pressure stepped structure is at present unknown, and may simply be a result of edge effects from the three-dimensional experiment. However, this structure may also be indicative of a late-time kinetic transformation that occurs at elevated pressures. Further simulations performed on two-dimensional geometries could help determine whether or not this is a geometry-dependent effect, or if it is indeed the signature of some late-time transformation.

Results from the present one-dimensional study have clearly shown that CeO_2 at an average initial porous density of 4.03 g/cm^3 remains in its ambient crystal structure, the cubic fluorite phase, during the course of shock compaction up to pressures of ∼12 GPa. Furthermore, the increased agreement observed by employing the three-phase EOS rather than the solid-liquid EOS lends credit to the claim that CeO_2 undergoes a shock-induced phase transition from the cubic fluorite phase to the orthorhombic phase, where equilibrium calculations indicate this to occur at ∼24 GPa. While the one-dimensional simulations do indeed lend some degree of insight into the high-pressure shock compression and EOS/phase behavior or CeO_2, several open questions remain. Specifically, it has yet to be determined experimentally what the threshold conditions for the cubic to orthorhombic transition are, and what role, if any, does morphology play in determining this threshold? Further, what type of transition, if it indeed is a transition, might the late-time step-like wave structure represent? Both require additional experimental and computational efforts.

1 Introduction

Particulate materials are, in general, a class of materials whose response to compressive loading is significantly more complicated than solids. In addition to the fundamental physical phenomena that occur as a result of compression in the particle itself (the solid component), one must also consider effects due to particle size, shape, surface features, and porosity, both internal and external to the particle. Add to this the possibility of undergoing modifications to the ambient crystal structure and/or stoichiometry, and a host of competing physics exist which may dominate the compression response at any given load. Such is the case for the shock loading of porous metal oxides like SiO_2,[1] CeO_2,[2] etc. Of paramount importance is determining the most prevalent physical mechanisms responsible for the measured bulk response, such that accurate modeling of these materials at high pressures and strain-rates can be achieved.

As a result, research efforts have been devoted to developing full-range equations of state (EOS) with the appropriate compaction model(s) that can capture both the low-pressure compaction and high-pressure EOS response of porous metal oxides. However, complicating these efforts is an oft realized lack of fundamental physical data by which one can validate a given EOS or compaction model. Consequently, certain simplifying assumptions must often be made in development or implementation of a computational model that may negatively effect the ability by which a given model can replicate experimental results.

This work examines the current equation of state and compaction model development for CeO_2, a metal oxide whose compression response from the porous state has recently been examined at high-strain-rates. A brief overview of the relevant EOS and compaction model formulations are presented first, detailing the underlying assumptions and/or simplifications that may effect model accuracy. Next, details of the high-strain-rate compression experiments are given, with emphasis placed on recent advancements in characterization of the initial sample configuration. Subsequently, details of the simulated experiments are presented, and simulated results employing the various EOS and compaction model implementations are compared to those obtained from experiment. Finally, conclusions are drawn with respect to our present ability to capture the complex response exhibited by CeO_2 under shock compression loading.

2 Theoretical Considerations

This section focuses on familiarizing the reader with how the solid-liquid and three-phase equations of state and the relevant P-α compaction model are developed and/or paramaterized for CeO_2. Full details regarding formulation of the solid-liquid and three-phase EOS construction can be found in Refs. [3, 4].

2.1 Solid-Liquid EOS

The solid-liquid EOS was developed to capture the phase behavior of CeO_2 assuming the material melts from its ambient cubic fluorite crystal structure. The EOS is constructed in a manner consistent with the standard SESAME database: it is designed to match experimental data at conditions near ambient and at moderate compressions (such as are reachable by single shocks) while behaving appropriately at the extreme limits of temperature and density. While constructs of this type have been proven effective for solid materials, highly porous materials can behave anomalously under shock compression, such that even under extreme compressive loading the material may never reach the ambient solid density.[5] Therefore, it may be that in the region of high pressures and moderate densities, where much of the data from shock experiments on porous materials lies, the physics underlying these types of EOS may be stressed considerably.

The solid-liquid EOS for CeO_2 is constructed as a three term Helmholtz free energy per unit mass:

$$F(\rho, T) = \phi(\rho) + F_{nuc}(\rho, T) + F_{elec}(\rho, T) \ , \quad (1)$$

where $\phi(\rho)$ represents the cold curve, or energy when the nuclei are at rest and the electrons are in their ground state; $F_{nuc}(\rho, T)$ captures the energy of moving nuclei while the electrons are still in their ground

state; and $F_{elec}(\rho, T)$ reflects the thermal energy when the electrons are excited and the nuclei are at rest. Thus, each of the three components in Eq. (1) capture a specific portion of the material response, which when combined yields the total EOS as a function of density, ρ and temperature, T.

Coverage of the full range of densities is handled by constructing the cold curve $\phi(\rho)$ from three separate potentials. The Lennard-Jones (LJ) potential is used at densities below the ambient density to represent the region of the liquid-vapor transition and vapor dome,[7] while at intermediate densities the Rose-Vinet (RV) potential is used.[8] The density at which the material switches from LJ to RV is kept as low as possible to allow the RV model to capture the measured isothermal bulk modulus and its pressure derivative (see measurements by Duclos et al.[9]) without interfering with the vapor dome. At higher densities starting at about twice the ambient, the Thomas-Fermi-Dirac (TFD) model is used.[10] At high densities in any material, the kinetic energy of the electrons dominates the energy of the material, and this contribution is correctly captured at high density by TFD.[11]

Coverage of the full range of temperatures is handled by the nuclear contribution $F_{nuc}(\rho, T)$. At temperatures below melt, the material is treated as a Debye solid; in the liquid regime, the model is modified to steadily lower the specific heat from a solid value of $3R$ per mole to the gas value of $3/2R$ per mole as temperature increases. The melt curve takes the Lindemann form, which requires as input the same Debye temperature required by the solid. The density dependence of the Debye temperature is determined by the Grüneisen parameter $\Gamma(\rho)$, the form of which guarantees that the parameter approaches 1 at low densities and 2/3 at high densities. The low-density limit guarantees proper behavior of the melt curve at low density, while the high-density limit again reflects the dominance of the kinetic energy over the potential energy, so Γ approaches the ideal gas value.[12] In this construction, only the nuclear model is aware that the material is in the solid or liquid state.

The final contribution to the free energy, $F_{elec}(\rho, T)$, is determined by performing a full TFD calculation over the entire density and temperature range of interest, and then subtracting the contribution from the $T = 0$ electrons (already included more accurately in the cold curve). For polyatomic materials like CeO_2, separate TFD calculations were performed on each of the atomic constituents, which were then combined via an additive volume mixing technique,[13] such that the constituents were in pressure and temperature equilibrium when mixed. The resultant EOS given by Eq. (1) is SESAME EOS 96170, and its isothermal pressure-volume (P-V) response is plotted with the experimental room temperature diamond anvil cell data of Duclos et al.[9] in Fig. 1. Good agreement is achieved between the solid EOS and experimental data in the region below the phase transition at 30-40 GPa.

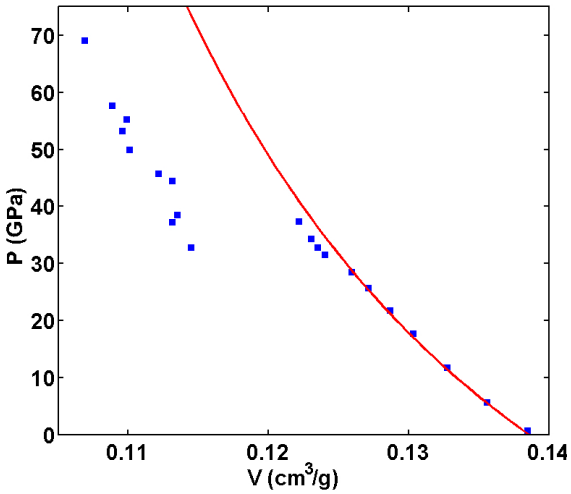

Figure 1: Isothermal (T = 298 K) pressure-volume response of solid CeO_2 predicted by SESAME EOS 96170 (solid line) shown with diamond anvil cell data of Duclos et al.[9].

A prevalent theme throughout the construction of the solid-liquid EOS is that material behavior is only well-defined in specific regions. To form a full-range EOS these regions must overlap, such that smoothing and/or interpolation functions must be applied. In the best case, these regions are small, as is the case in joining the LJ and RV potentials. However, more often is the case that these interpolation re-

gions are quite large, with well-defined regions being located only at ambient and the extremes of compression and/or temperature, e.g. the Grüneisen function. In instances such as this, the form of the chosen smoothing function and the parameters defining it constrain the EOS in the extrapolated regions. As a result, interpolation functions must only be applied over regions of phase space where sharp deviations in the material behavior are not expected.

2.2 Three-Phase EOS

The three-phase EOS has many of the same constructs as the solid-liquid EOS discussed in Sect. 2.1, and as a result is not covered in as much detail here. In the case of the three-phase EOS three separate EOS are defined explicitly, the ambient structure solid, the high-pressure solid, and the liquid phase EOS, where the liquid phase is modeled off the low-pressure solid phase. The stability of each phase is determined by minimization of the Gibbs free energy, and all phases are combined into a single SESAME table. It should be noted that, while not employed in the current SESAME EOS table, this type of construction lends itself to implementation into kinetic models that allow for time- and/or rate-dependent transitions between the phases.

The low-pressure solid phase is again the cubic fluorite phase and is described with a three-term Helmholtz potential comprised of a cold component, $\phi(\rho)$, a thermal nuclear component, $F_{nuc}(\rho, T)$, and a thermal electronic component, $F_{elec}(\rho, T)$, see Eq. (1). While exact values for the parameters have changed slightly to better match available experimental data, the cold curve is similarly represented by the Lennard-Jones, Rose-Vinet, and Thomas-Fermi-Dirac forms with interpolation functions connecting the segments. Furthermore, in the three-phase construction the thermal electronic component has been set equal to zero to better align with experimental specific heat data.[3]

The high-pressure solid phase is the orthorhombic phase and is defined primarily through room-temperature isothermal data,[9] which yields information about the location of the phase boundary, bulk modulus, and behavior of the density at pressure. Similar to the low-pressure solid, the high-pressure solid is defined with a three-term Helmholtz potential with the same forms of the cold-curve and nuclear models, the only difference being different values are defined for the model parameters. The electronic contribution to the Helmholtz potential for the high-pressure solid is modeled as it was in the low-pressure solid, with an additive volume mixture technique.

The liquid phase is also defined using a three-component Helmholtz potential. For this phase, the cold curve is defined by that of the low-pressure solid with an additive term to reflect the entropy of melting and density dependence of the melt temperature to ensure the Gibbs free energy of the liquid is always higher than the solid at low temperatures. The nuclear model is the same as that for the low-pressure solid, with the exception that the extra configurational entropy attributed to melting is set to $\Delta S = 0.8\ k_B$/atom, where k_B is the Boltzmann's constant. The final contribution to the Helmholtz potential is the electronic contribution, and it is defined in the same manner as the high-pressure solid, as the liquid phase extends over the entire density range of the EOS, though it is not always the stable phase.

Each of these three EOS, the low-pressure solid, the high-pressure solid, and the liquid, are combined into a single SESAME EOS table using the procedure outlined in Ref. [14]. The mass fraction of a given phase is determined at each density and temperature on the SESAME grid which minimizes the Gibbs free energy while maintaining pressure equilibrium. This is an iterative process whereby the partial volumes of each phase are adjusted to achieve pressure equilibrium first, then the mass fractions of each phase are subsequently adjusted to minimize the Gibbs free energy. The process is repeated until the equilibrium mass fractions and partial volumes are achieved, resulting in SESAME EOS 96171. The isothermal compression response of the solid calculated from three-phase EOS is shown alongside room temperature diamond anvil cell data for CeO_2 in Fig. 2, where good agreement is observed in both the low-pressure and high-pressure solid regimes.

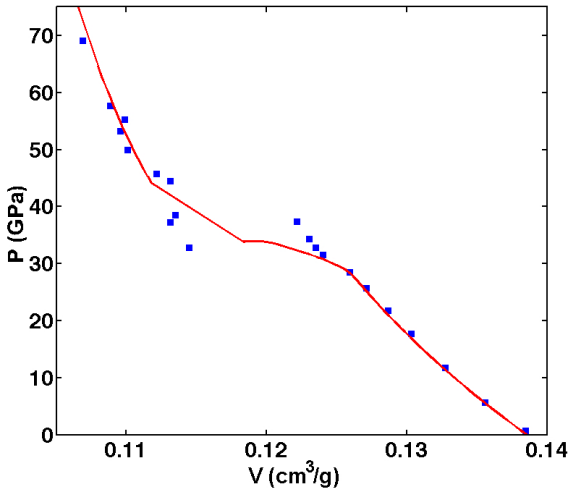

Figure 2: Isothermal (T = 298 K) pressure-volume response of solid CeO_2 predicted by three-phase SESAME EOS 96171 (solid line) shown with diamond anvil cell data of Duclos et al.[9].

2.3 P-α Compaction Model

The P-α model[15, 16] is commonly used to describe the response of initially porous materials subjected to shock loading. In this model $\alpha(P)$ is a measure of distention, and is described by the relationship $\alpha(P) = V/V_{SP}$, where V is the volume of the porous material and V_{SP} is the volume of the solid at the same pressure, P, and energy, E. The P-α model was originally developed to describe the compaction behavior of ductile porous materials under dynamic (shock) loading, and decomposed the compaction process into separate elastic and plastic components. While many different formulations for $\alpha(P)$ exist,[17] the implementation examined in the current work considers pore collapse to be controlled entirely by the plastic response through:

$$\alpha(P) = 1 + \sum_{i=1}^{n} a_i e^{-b_i P} \ , \tag{2}$$

where the coefficients a_i and b_i are empirical constants determined by matching to shock wave data. Assumptions in the P-α model are that (a) shear strengths are neglected, and (b) specific internal energy for the porous and solid materials are equivalent under identical conditions of pressure and temperature. Neglecting shear strength of the powders limits the model to describe only the irreversible process of compaction through the closure of voids, and constrains the stress tensor to be spherical such that only global pressures are considered. By neglecting the surface energies of the pores, the second assumption favors porous systems composed of large particles. In fact, it has been shown that as particle size enters the nano-regime surface energies can significantly influence the compaction response[18].

Historically, the P-α model has been successfully applied to a wide range of ductile porous metals, and it is particularly well-suited for systems with low levels of porosity, where the materials are not expected to behave anomalously, see Sect. 2.1. In addition, Hugoniot data for solid metals are often readily available, and application of a Grüneisen equation of state (EOS) is sufficient for predicting the porous Hugoniot. For less well characterized materials like porous oxides and other metastable materials, the Hugoniot of the solid may not be known, nor may a simple Grüneisen EOS be sufficient to predict the porous Hugoniot response if the solid is known. This is especially true for materials with high levels of initial porosity. As such, one may be unable to determine $V_{SP}(P)$ along the fully densified porous Hugoniot to correctly define $\alpha(P)$. As a result, simplifications based on the initial solid density or the solid Hugoniot can be made when defining $\alpha(P)$, such that one may have:

$$\alpha_1 = V/V_0, \tag{3}$$

$$\alpha_2 = V/V_{SS}, \tag{4}$$

$$\alpha_3 = V/V_{SP}, \tag{5}$$

where Eqs. (3), (4), and (5) increase in their level of sophistication for defining $\alpha(P)$. A schematic illustrating the different reference curves on which the definitions for $\alpha(P)$ given in Eqns. (3)-(5) is shown in Fig. 3. In Eq. (3) α_1 is calculated using the initial volume of the solid material, V_0, where in Eq. (4)

α_2 is calculated from the volume of the initially solid material at the corresponding pressure, V_{SS}. Lastly, Eq. (5) calculates α_3 in the appropriate manner by using the volume of the solid material at the corresponding pressure and energy, i.e. along the porous Hugoniot.

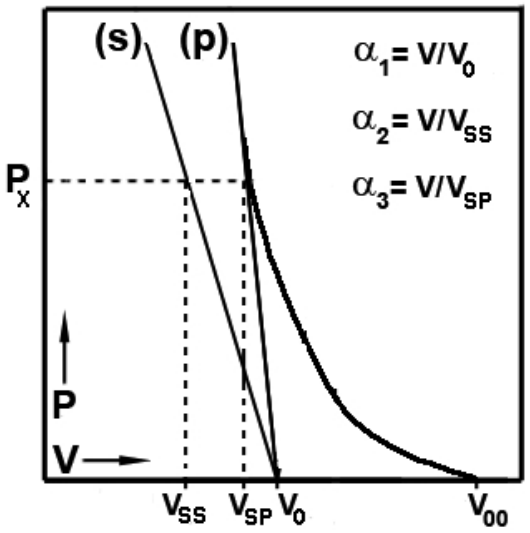

Figure 3: Schematic illustrating the different reference curves for $\alpha(P)$ calculations. Curves (s) and (p) denote the solid and porous Hugoniots, respectively, and the P-α crush curve is shown to begin at a porous volume V_{00}.

3 Experimental Considerations

The primary method of validation for any EOS or compaction model is through comparison with experimental results. As a consequence, one must have confidence in the fidelity of experimental data and the corresponding limits of uncertainty in those measurements. With regard to validating the solid-liquid and three-phase EOS for CeO_2, satisfactory agreement has been shown for isothermal data (See Figs. 1 and 2). However, experimental Hugoniot data on solid CeO_2 does not exist, and further validation of both 96170 and 96171 must come from comparisons with porous data. Recent advancements in experimental techniques and analysis methodologies for collecting and reporting porous Hugoniot data have resulted in marked improvements to data fidelity, where the most significant improvements have been in characterization of the initial sample configuration. Specifically, the initial porous density and sample thickness are known with much higher degrees of accuracy than was possible using previous methods.[19] A full description of the experimental methods and analysis techniques applied to CeO_2 can be found in a corollary work by Fredenburg et al.[2]

In the new method powder samples of CeO_2 were loaded to approximately 55% of theoretical maximum density in the target fixture shown in Fig. 4. In this configuration impact of the target with a high-speed projectile carrying a Cu impactor occurred from the left with respect to Fig. 4(a) and (b). The powders were pressed directly into the assembled Cu baseplate and stainless steel cylinder assembly with a punch composed of high strength tool steel. During pressing, the entire fixture was located in an alignment die to assure the axis of the punch (not shown in Fig. 4) was aligned with that of the cylinder, resulting in a pressed powder sample that was as flat as possible. Following pressing, the target was removed from the alignment die and measurements of the powder thickness were made at the sample center, along the outer diameter of the sample at the axes, Φ_{CP}, and at each of the velocimetry probe locations, Φ_{VP} (see Fig. 4 (c) and (d)). Additional measurements were also made at the same locations on the front surface of the Cu baseplate to characterize any bowing that may have occurred in the baseplate as a result of sample pressing.

This newly developed pressing and characterization technique allowed for determination of shock arrival times at the probe locations to within ~1 ns, and corresponding powder thicknesses to within ±1-2 μm. As a result, shock velocities through the powder compact (measured at 1-3 locations per experiment) could be resolved with unprecedented accuracy. These methods also permitted tighter control over the initial sample density. Taken with the measured impact velocity of the experiment, which was typically known to better than 1%, the measured shock velocity and initial density of the sample were

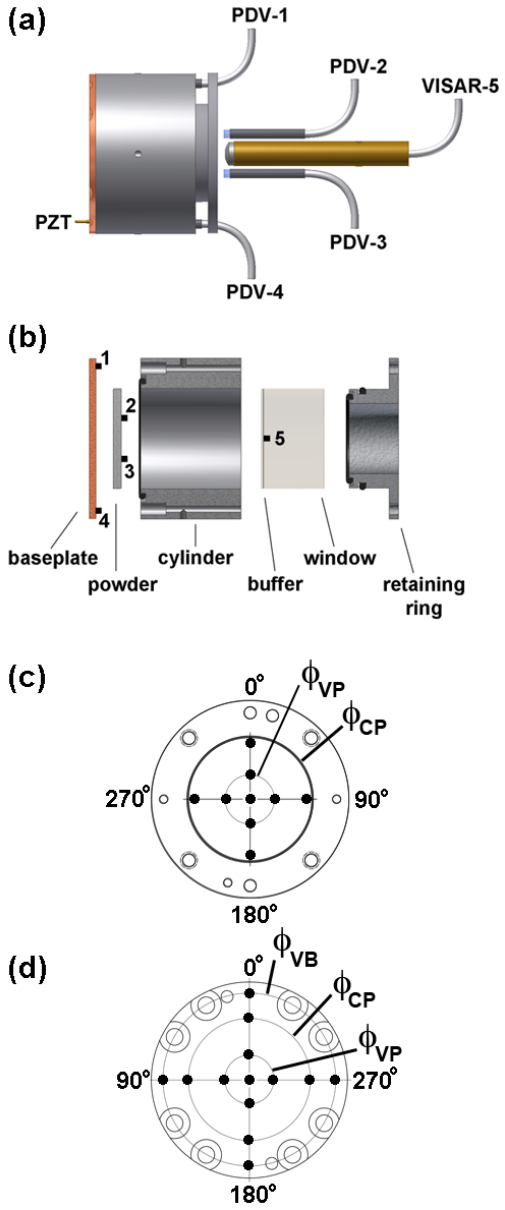

Figure 4: (a) Assembled and (b) expanded experimental target configuration illustrating velocimetry measurement locations (numbers) and corresponding probes. Also shown are locations where metrology was performed on the (c) powder rear surface and (d) baseplate impact surface. Diameters Φ_{VP}, Φ_{CP}, and Φ_{VB} are the powder probe diameter, inner cell diameter, and baseplate probe diameter, respectively.

used in impedance matching calculations to determine the remainder of the shocked state, i.e. the material velocity, u_P, stress, P, and specific volume, V or density, $\rho = 1/V$. Standard uncertainty calculations for impedance matching with two materials (solid impactor striking a solid target) were extended for the porous configuration shown in Fig. 4 (solid impactor striking a solid target transmitting the shock into a porous material) in Ref. [2], and have been applied to the CeO_2 results considered in the present investigation. Results obtained from experiments are given in Table 1, where three separate morphologies of CeO_2 (300 nm, equiax, and rods) were tested.

4 Problem Set-Up

Validation of the previously discussed equations of state and compaction model were undertaken by performing one-dimensional hydrocode simulations of the inherently three-dimensional shock compaction experiments. Location of the one-dimensional representation of the experiment was along the center line of the geometry shown in Fig. 4. With this approach, one can determine the Hugoniot state of the simulation for comparison with experiment, as well as examine characteristics of the computed and measured propagated wave profiles. It is not expected that the one-dimensional approach will be able to capture late time effects in the measured wave profiles, as these are likely a result of the three-dimensional nature of the experiment. However, simulated results will be able to determine how well a combined EOS and compaction model can capture the initial Hugoniot state. Results will also be able to lend insight into the effects of release and edge waves in the measured wave profiles, thereby guiding future design of experiments.

The Lagrangian/ALE hydrocode FLAG[20] was used to model the experiments in one-dimension, where direct comparisons are made between simulated and experimental Hugoniot states and propagated wave profiles for equations of state 96170 and 96171 combined with the P-α model defined by Eqns. (2)-(5). Prior to performing the full suite of simulations, it is necessary to discuss properties of the simulated materials and examine the sensitivity

Table 1: Experimental results for dynamic experiments on three morphology CeO_2 powders, 300 nm, equiaxed, and rods (micrographs of the three morphology powders are given in Fig. 18). In these experiments the initial density ρ_{00}, impact velocity V_I, and shock velocity U_S were measured, and the stress P, material velocity u_P, and density ρ were calculated. Values within () next to ρ_{00} denote the total spread in initial density, which is not symmetric about the reported value. Shots with an * indicate experiments where release overtake of main compaction front occurred prior to arrival of the shock at the U_S measurement location.

Shot	ρ_{00} (g/cm^3)	V_I (km/s)	P (GPa)	u_P (km/s)	U_S (km/s)	ρ
300 nm						
56-11-20*	4.039 (.252)	0.219 ±.001	0.801 ±.044	0.196 ±.002	1.011 ±.004	5.013 ±.174
56-11-19	4.023 (.138)	0.407 ±.001	1.817 ±.165	0.356 ±.004	1.269 ±.077	5.593 ±.170
56-11-56	4.033 (.150)	0.689 ±.001	3.915 ±.342	0.582 ±.007	1.669 ±.093	6.191 ±.221
1S-1525	4.012 (.090)	0.782 ±.003	4.587 ±.241	0.657 ±.007	1.740 ±.047	6.448 ±.143
Equiaxed						
56-12-01	4.028 (.070)	0.394 ±.001	1.724 ±.177	0.346 ±.005	1.239 ±.092	5.587 ±.160
56-12-13	4.010 (.186)	0.691 ±.001	3.776 ±.478	0.587 ±.010	1.603 ±.139	6.330 ±.340
56-12-06	4.044 (.114)	0.768 ±.001	4.366 ±.284	0.649 ±.007	1.663 ±.065	6.632 ±.197
2S-648	4.037 (.033)	2.271 ±.036	24.11 ±2.85	1.710 ±.041	3.492 ±.228	7.912 ±.400
Rods						
56-11-26*	4.023 (.114)	0.146 ±.001	0.513 ±.032	0.131 ±.002	0.971 ±.033	4.652 ±.046
56-11-27	4.052 (.178)	0.405 ±.001	1.775 ±.079	0.355 ±.003	1.233 ±.012	5.692 ±.153
56-11-55	4.020 (.143)	0.669 ±.001	3.666 ±.263	0.568 ±.006	1.605 ±.069	6.224 ±.189
1S-1523	4.055 (.066)	0.770 ±.015	4.572 ±.348	0.646 ±.015	1.747 ±.028	6.433 ±.171
2S-589	4.031 (.079)	1.486 ±.037	12.56 ±1.23	1.168 ±.033	2.666 ±.062	7.175 ±.285
2S-594	3.975 (.093)	2.289 ±.040	24.62 ±3.32	1.718 ±.046	3.606 ±.262	7.592 ±.451
2S-593	4.036 (.041)	2.984 ±.052	38.55 ±4.21	2.157 ±.053	4.428 ±.233	7.869 ±.349
69ts-12-09	4.033 (.090)	3.657 ±.019	52.34 ±5.41	2.605 ±.048	4.982 ±.305	8.453 ±.494
69ts-12-23	4.069 (.189)	4.560 ±.010	77.84 ±9.43	3.137 ±.066	6.098 ±.421	8.380 ±.585
69ts-12-17	4.016 (.160)	5.601 ±.012	108.8 ±15.4	3.787 ±.093	7.158 ±.597	8.526 ±.706

of results on the chosen mesh size, artificial viscosity, and the so-called "impedance matching" of neighboring cells with different material definitions.

4.1 Material Properties

One-dimensional simulations were performed such that all of the major components of the experimental setup were captured. As such, the sabot material, which was composed of either Al or Lexan, the impactor and baseplate, which were both OFHC Cu, the CeO_2 powder, and the window, which was either PMMA or LiF, were modeled explicitly. In all material definitions the initial sound speed in a given material was set to 1 x10^{-5} km/s. Details of the equation of state (EOS) and strength parameters chosen for the simulated materials is given in the paragraphs that follow.

For experiments whose impact velocities were less than 1 km/s, the sabot was composed of an Al 6061 alloy. The corresponding material was simulated with solid elements, whose volumetric response was assigned the Al SESAME EOS 3720 with an initial solid density of 2.70 g/cm^3. Strength was modeled with a PTW strength model,[22] where the parameters chosen were those of Chen and Gray III.[23] Density dependence of the melt temperature was assigned through EOS 33720. The Cu impactor and baseplate were also modeled using solid elements with the SESAME EOS for Cu, 3336. Initial solid density of the Cu was 8.93 g/cm^3, and the PTW strength model was used to describe the deviatoric response.[23] Variation in the melt temperature and shear modulus with increasing density were represented by EOS 33336 and 33330, respectively.

The CeO_2 powder was modeled as a gas, and as such, no explicit strength model was assigned to the cell elements. The volumetric EOS response was captured with 96170 for the solid-liquid material and with 96171 for the three-phase material. In all instances the initial density of the powder was set to 4.03 g/cm^3, and the crush response was modeled using the 2-term exponential P-α crush model as defined in Sec. 2.3.

For the window material, separate definitions were given to the PMMA and LiF windows, where for both materials the window was modeled with solid elements. For the PMMA windows the volumetric response was assigned to SESAME EOS 7741, the polycarbonate (lexan) EOS. Polycarbonate was chosen because an explicit EOS for PMMA does not exist in the SESAME library. The corresponding polycarbonate initial solid density of 1.196 g/cm^3 was used. Strength properties of PMMA were assigned with the isotropic elastic/plastic model where the shear modulus, melt temperature, and yield strength were defined using the properties of Rosenberg et al.[24] The melt temperature variation with density was captured with EOS 37741. For experiments with impact velocities greater than 1 km/s, PMMA was also used as the sabot material with the aforementioned material definitions. For the LiF windows SESAME EOS 7271 was used to define the volumetric response of the elements, and no strength model was specified. Variation in the melt temperature with density was assigned through EOS 37271.

4.2 Mesh Size

Advancements in characterization techniques have allowed for thicknesses of the sample and target to be measured to within ±1-2 μm. However, computational cost is inversely related to the size of the mesh, and as a result one must balance computational efficiency with the ability to accurately capture the physics of the problem of interest. A practical limit on the minimum size of the mesh is due to the continuum nature of the physics being modeled, i.e. mesh sizes on the order of several atoms nullifies the continuum approximation. In a similar context, an upper limit is set by the fact that in typical finite element calculations the numerical width of the shock front is usually between 3-5 elements thick.[21] Therefore, to resolve details of the propagating wave structure through porous CeO_2, there must be a sufficient number of elements across the sample thickness such that the wave can reach a steady state as it traverses the powder.

In the current analysis, a uniform mesh was assigned to the problem with mesh sizes of 2.5, 5, 10, 20, and 40 μm, and each were run on three simulated experiments at low (0.770 km/s), moderate (2.984

km/s), and high (5.601 km/s) impact velocities, to determine the effect of varying the mesh size on the resultant Hugoniot state and propagated wave profile. For consistency, all simulations were run on four processors, and the maximum time step was set to 10^{-4} μs, with the exception of the highest velocity simulation with a mesh size of 2.5 μm, which required the maximum time step be decreased to 10^{-6} μs. In the mesh study SESAME EOS 96170 with a two-term exponential P-α model was used for all tests, where $\alpha(P)$ was defined by Eq. (3). The results of this study are given in Table 2 and plots of the wave profile as it enters and exits the powder are shown in Fig. 5. Artificial viscosity parameters for all materials were kept constant in studying the effects of mesh size.

Table 2: Total elapsed simulation run time, measured shock velocity, and 10-90% rise times for input (I.R.T.) and propagated (P.R.T.) waves in the powder for mesh sizes of 2.5, 5, 10, 20, and 40 μm.

Mesh	2.5 (μm)	5 (μm)	10 (μm)	20 (μm)	40 (μm)
1S-1523, V_I = 0.770 km/s					
Time (s)	6676	1764	487	144	49
U_S (km/s)	1.71	1.70	1.71	1.51	1.77
I.R.T. (ns)	11	20	36	71	155
P.R.T. (ns)	10	24	44	96	129
2S-593, V_I = 2.984 km/s					
Time (s)	6338	1622	432	126	41
U_S (km/s)	4.79	4.78	4.78	4.77	4.87
I.R.T. (ns)	1	2	4	9	15
P.R.T. (ns)	1	3	6	11	17
69ts-12-17, V_I = 5.601 km/s					
Time (s)	N/A	3742	966	265	82
U_S (km/s)	8.14	8.14	8.13	8.16	8.13
I.R.T. (ns)	1	1	1	3	5
P.R.T. (ns)	1	1	1	2	6

The simulation run times in Table 2 clearly show that as mesh size increases from 2.5 μm to 40 μm, computational time decreases significantly. For the highest impact velocity with the finest mesh, the simulation was unable to run to completion after 8400 s; however, examination of the low and moderate velocity simulations shows that increasing the mesh size

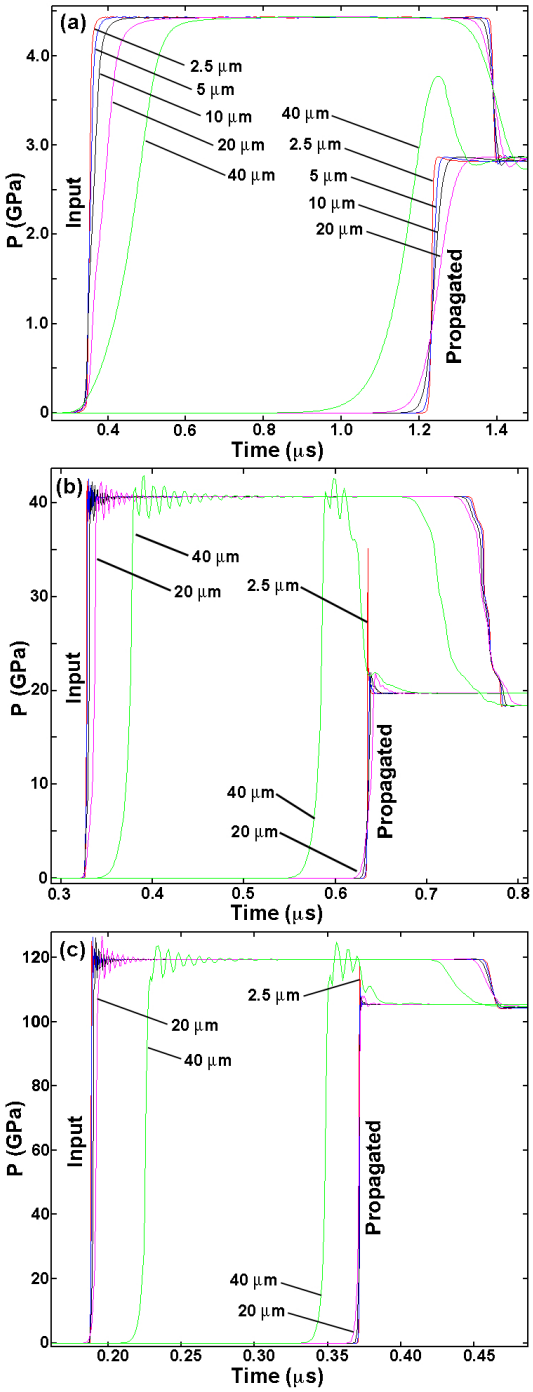

Figure 5: Pressure profiles showing input and propagated wave traces as a function of mesh size for experiments (a) 1S-1523, (b) 2S-593, and (c) 69ts-12-17.

from 2.5 μm to 5 μm reduces the total computational time by nearly 75%. Shock velocities reported in Table 2 were measured using the time of arrival of the input and propagated waves at 50% of the equilibrated peak pressure. Similarly, the input and propagated rise times (I.R.T. and P.R.T.) were calculated from the difference in the time it took for the wave to increase from 10% to 90% of its peak equilibrated state. At low and moderate impact velocities, the shock velocity remains relatively consistent for the 2.5, 5, and 10 μm mesh sizes, where greater deviations are observed as the mesh increases to 20 and 40 μm. Inspection of Fig. 5(a) and (b) reveals that for these two larger mesh sizes the wave profiles are significantly more disperse than those at a finer mesh, likely reflecting the earlier argument that the shock rise time must occur over several elements.[21] Supporting this argument is the finding that in all measurable instances, increasing the mesh size is shown to result in an increase in the 10-90% risetime of the simulation.

Another mesh dependent feature observed in Fig. 5 is the initial pressure overshoot past the equilibrated state in the propagated trace. This is observed for the 40 μm mesh at all impact velocities, and for the 20 μm mesh at intermediate velocity. In addition, the finest mesh size of 2.5 μm also displays this overshoot at moderate and high velocities, though in this case the overshoot is restricted to a short time-duration spike, see Fig. 5(b) and (c). While altering the values chosen for artificial viscosity are expected to effect the degree to which this overshoot occurs, the present analysis suggests that too fine and too course of a mesh result in spurious behavior of the propagated wave profile. As a result of these findings and to achieve a balance between computational accuracy and computational efficiency, the authors have chosen a mesh size of 5 μm for all further simulations.

4.3 Artificial Viscosity

In the previous section, the effect of mesh size was examined by keeping the artificial viscosity constant. In this section, the mesh size is kept constant at 5 μm and the artificial viscosity is varied to determine its effect on the Hugoniot state and measured wave profiles. In the present analysis artificial viscosity is assigned to three separate material blocks, the sabot (Lexan or Al), impactor (Cu), and baseplate (Cu) , the powder (CeO_2), and the window (Lexan of LiF). Specifically, the effects of varying the linear and quadratic coefficients of artificial viscosity under compression, q_1 and q_2, as well as the linear term under tension, q_{1n}, are examined. In addition to the standard linear and quadratic terms, a Barton side form of the artificial viscosity with the standard settings was included in all of the simulations.

4.3.1 Sabot, Impactor, and Baseplate

Here the effects of varying q_1, q_2, and q_{1n} in the sabot, impactor, and baseplate are examined, while keeping the artificial viscosity constant in the powder and window at $q_1 = 0.30$, $q_2 = 1.5$, and $q_{1n}= 0.10$. Results from these simulations are shown in Fig. 6. The compression terms q_1 and q_2 are expected to have the greatest effect during the initial rise to peak pressure, as that is where, under compression, the hydrodynamics may experience the greatest amount of numerical instability due to the rapid rise to the peak state. As such, Fig. 6(a) and (b) focus on the region near initial shock breakout.

Examination of Fig. 6(a) shows that for all impact velocities simulated, increasing q_1 from 0.10 to 0.35 has two effects. The first is that at low values of q_1 the pressure trace is observed to rise past the equilibrium state, where the overshoot becomes negligible between $q_1 = 0.20$ - 0.25. The second effect of increasing q_1 is to cause the initial shock front to spread out, with the lowest values of q_1 having the shortest duration 10-90% risetimes. Therefore, to keep the shock wave as steep as possible while still not permitting an unrealistic overshoot in the initial pressure a value of $q_1 = 0.20$ was selected as optimal for the sabot, impactor, and baseplate. With respect to increasing q_2 from 0.10 to 2.5, similar trends with respect to the initial pressure spike and a fanning out of the wave front were observed. For the velocity and pressure ranges of interest to the current investigation, inspection of Fig. 6(b) reveals that an optimal value for q_2 is 1.0.

The tensile component of the artificial viscosity q_{1n}

had the greatest effect on the falling portion of the wave following equilibration at the peak state. However, for the simulations examined the effect of varying q_{1n} from 0.05 to 0.30 on the release profile was still quite small, on the order of several nanoseconds. Without the presence of obvious numerical instabilities or the ability to directly validate the release profiles from experiment, q_{1n} was arbitrarily chosen at an intermediate value of 0.15.

4.3.2 CeO_2 Powder

Having defined the appropriate artificial viscosity parameters for the solid sabot, impactor, and baseplate in the previous section, a similar study is undertaken to determine the appropriate parameters for the porous CeO_2. To isolate the effects of modifying the artificial viscosity on the powder, values for the sabot, impactor and baseplate were kept constant at $q_1 = 0.20$, $q_2 = 1.0$, and $q_{1n} = 0.15$, and those for the window also remained fixed at $q_1 = 0.3$, $q_2 = 1.5$, and $q_{1n} = 0.10$. The resultant pressure profiles for the wave as it enters and exits the powder are shown in Fig. 7, where in all instances the propagated pressure profile has been shifted in time to allow for simultaneous viewing of both the input and propagated traces.

The effect of q_1 was examined by varying q_1 from 0.10 - 0.35, while keeping q_2 and q_{1n} fixed at 1.5 and 0.1, respectively. The resulting pressure profiles are shown in Fig. 7(a). In all instances increasing q_1 caused an increase in the 10-90% risetime of the wave, increasing by as much as 12 ns and 6 ns for the input and propagated pressure traces for the lowest impact velocity shot, 1S-1523. For the two higher impact velocity shots, risetimes differ by a nanosecond or less. Pressure oscillations are observed in the input trace as impact velocity is increased, Fig. 7(a-2) and (a-3), and the magnitude of these oscillations decreases with increasing q_1. For the corresponding propagated traces a pressure overshoot is observed at low values of q_1, which disappears as q_1 is increased to 0.35. In an effort to keep the propagated wave as steep as possible at the lower impact velocities, while still maintaining minimal pressure oscillations and overshoot at higher impact velocities, it was decided that separate values of q_1 would be assigned to the porous material depending on the impact velocity of the simulation. For impact velocities less than 1 km/s $q_1 = 0.10$, and for those above 1 km/s $q_1 = 0.35$.

The quadratic artificial viscosity term was then varied from $q_2 = 0.5$ - 3.0 with the aforementioned impact velocity dependent values of q_1 assigned, and $q_{1n} = 0.1$. These results are shown in Fig. 7(b). Increasing q_2 resulted in a slight dispersion of the input and propagated wavefronts, causing 10-90% risetimes to increase by approximately one nanosecond or less. For the lowest velocity simulation, Fig. 7(b-1), this was the only observable effect of changing q_2. The greatest effect of modifying q_2 was observed on the two higher impact velocity shots where reduced ringing in the input pressure trace following the initial rise to the peak shocked state occurred, see Fig. 7(b-2) and (b-3). In these simulations the initial pressure oscillations are reduced to less than 5% with $q_2 = 2.0$, where increasing q_2 further resulted in minimal improvements in oscillation reduction. For the propagated traces the lowest value chosen for q_2 resulted in a pressure overshoot following the initial rise and a slight delay in the arrival time of the wave with respect to all other values of q_2 chosen. To reduce the magnitude of the pressure oscillations in the input trace and to eliminate the overshoot and delay in the propagated trace, a value of $q_2 = 2.0$ was set for the powder for all further simulations.

The final artificial viscosity parameter investigated for the powder was q_{1n}, where q_{1n} was varied between 0.05 - 0.30 while keeping all other viscosity parameters constant. Results from this investigation are shown in Fig. 7(c). In all instances, a noticeable variation in the pressure traces were only observed in the release portion of the input wave, and as such, that is the only portion of the wave profiles shown in Fig. 7(c). For each of the simulated impact velocities, increasing the value of q_{1n} resulted in greater dispersion in the release wave, such that an inflection point is observed at all velocities. This is demonstrated by the change in directionality of the arrows in Fig 7(c-1), (c-2), and (c-3). Furthermore, each of the chosen values of q_{1n} produces a release profile with no obvious pressure spikes or oscillations. Without values for the sound speed at pressure by which to compare

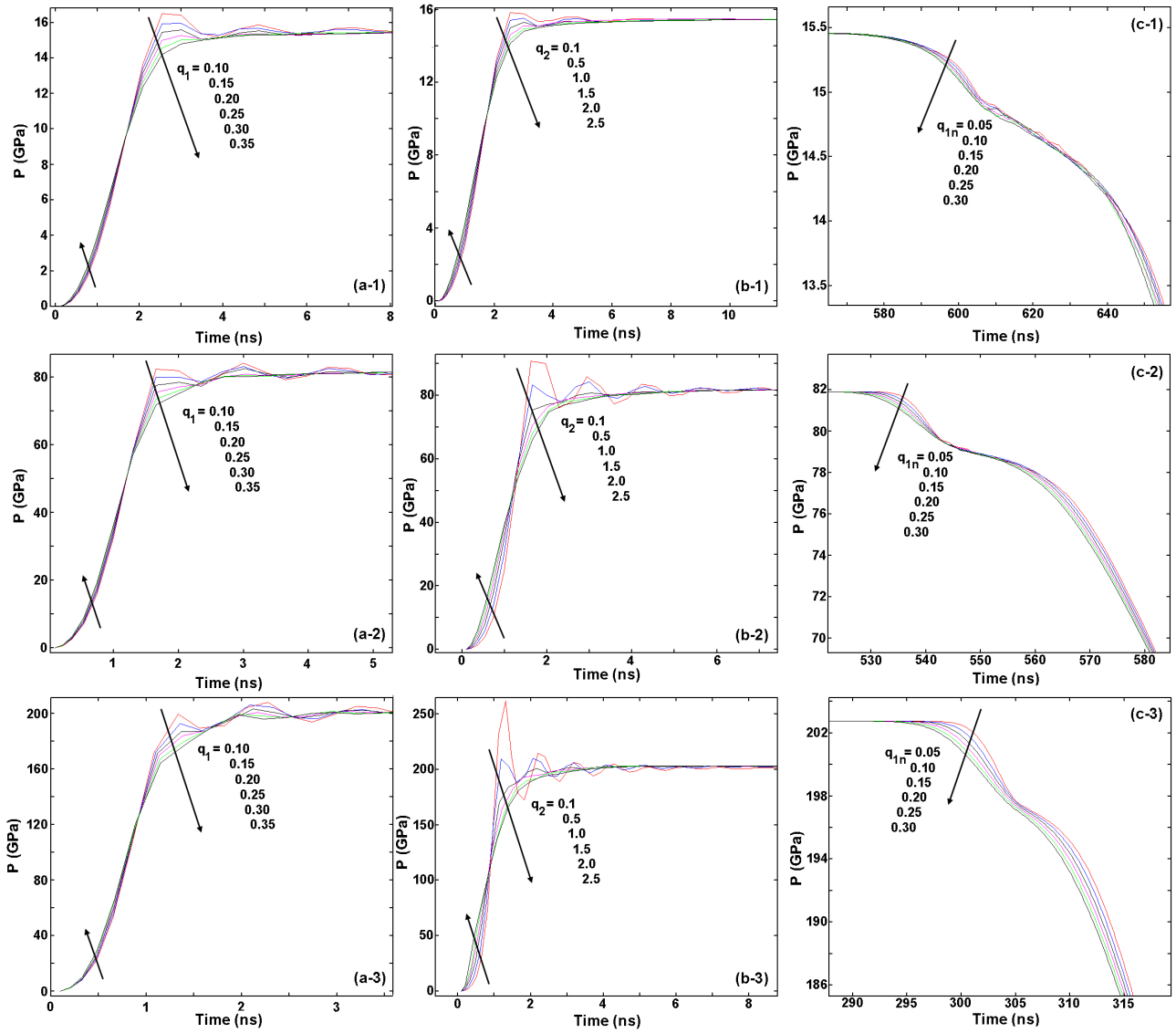

Figure 6: Effect of varying artificial viscosity parameters on the Cu baseplate and impactor and the sabot (Al or Lexan) on the pressure profiles for a tracer particle near the Cu-Cu impact plane. Varied parameters are (a) the linear compression coefficient q_1, (b) the quadratic compression coefficient q_2, and (c) the linear tensile coefficient q_{1n}. Trailing numbers -1, -2, and -3 correspond to the low, medium, and high impact velocity simulations, 1S-1523, 2S-593, and 69ts-12-17, respectively.

the release profiles to at this time, the value for q_{1n} is arbitrarily set to 0.15, as it was in the previous case for the sabot, impactor, and baseplate.

4.3.3 Windows, PMMA and LiF

The final component for which the effect of artificial viscosity was examined explicitly was the window material, which depending on the impact velocity of the experiment/simulation was wither PMMA or LiF. In this portion of the investigation the artificial viscosity parameters for the sabot, impactor, and baseplate were kept constant at the optimal values determined earlier, $q_1 = 0.20$, $q_2 = 1.0$, and $q_{1n} = 0.15$. Similarly, those for the powder were also kept constant at $q_1 = 0.10$ for impact velocities less than 1 km/s and $q_1 = 0.35$ for all those above, and $q_2 = 2.0$ and $q_{1n} = 0.15$ for all impact velocities. The effect of varying the artificial viscosity parameters on the window is shown in Fig. 8, where (if shown) the propagated pressure trace has been shifted in time to allow for simultaneous observation.

The linear coefficient in compression q_1 was varied in the window material from 0.10 - 0.35. At low and moderate impact velocities, varying q_1 is shown to have very little effect on the pressure profile at the Powder-Window interface (left-hand traces in Fig. 8(a-1) and (1-2)), while having a stronger influence on the pressure profile after the wave has propagated through the window 0.5 mm. Similar to its effect on the previous materials investigated, lower values of q_1 sometimes resulted in an initial pressure overshoot, such that a good combination of a sharp wavefront with minimal overshoot was achieved by setting $q_1 = 0.20$. For both the PMMA and LiF material components, a value of $q_1 = 0.20$ was chosen for all further simulations.

The quadratic coefficient q_2 had a stronger effect on the ringing behind the initial front, and examination of the propagated pressure profiles for all simulations shown in Fig. 8(b) illustrate the increased degree of ringing that occured when q_2 was set to low values. The optimal value of q_2 chosen for all experiments was $q_2 = 1.5$. The final artificial viscosity parameter investigated for the window was the linear coefficient in tension, q_{1n}. Overall, varying q_{1n} had very little effect on the pressure profiles in the window material, as illustrated in Fig. 8. In the previous materials the effect of varying q_{1n} was best observed in the falling portion of the wave following the equilibrated peak pressure. However, the corresponding portion of the waves in the window materials appeared nominally similar such that a distinction of the various q_{1n} values could not be made. Instead, the initial portion of the wave, immediately following the rise to the peak state was examined, and Fig. 8 shows that varying q_{1n} from 0.05 - 0.30 resulted in pressure profiles that were similar to one another by less than 0.5 GPa for all impact conditions. Therefore, all values of q_{1n} investigated describe the pressure profile in a nominally similar fashion. To remain consistent with the previous q_{1n} assignments, a value of $q_{1n} = 0.15$ was chosen for the window materials.

4.4 "Impedance Matching"

The concept of impedance matching has historically been applied to mesh zoning where numerical instabilities in the shock profiles may occur due to the propagation of the shock through an interface bounded by two materials with largely different densities. In the current problem these interfaces exist at the Sabot-Impactor, Baseplate-Powder, and Powder-Window boundaries. Optimization of the artificial viscosity parameters has removed much of the instabilities from these interfaces except, possibly, those at the Baseplate-Powder interface. As a result, "impedance matching" will only be investigated at this interface.

Within the context of mesh zoning, "impedance matching" refers to the product of the material density and the mesh size, which in the current one-dimensional problem is defined as:

$$\rho_1 \Delta x_1 = \rho_2 \Delta x_2 \ , \tag{6}$$

where ρ_i and Δx_i are the initial density and element thicknesses for the materials on either side of the interface. It should be noted that the relation given by Eq. (6) contrasts with the shock impedance, which is generally defined as the product of the initial sample density and the shock wave velocity, $\rho_0 U_S$.[25]

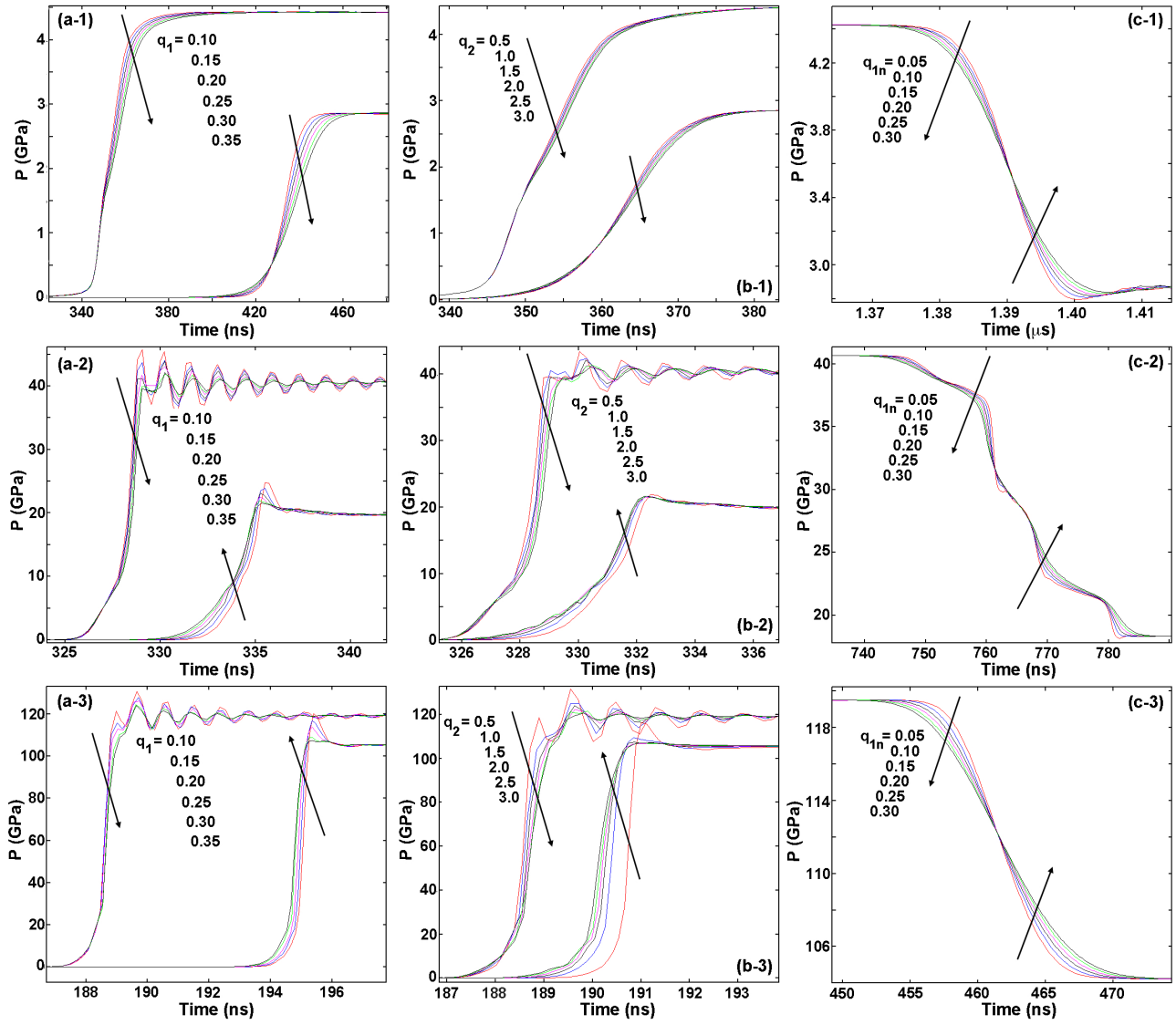

Figure 7: Effect of varying artificial viscosity parameters on the CeO_2 powder material showing pressure profiles for a tracer particle one element away from the Cu-Powder impact plane and another tracer one element from the Powder-Window impact plane. Varied parameters are (a) the linear compression coefficient q_1, (b) the quadratic compression coefficient q_2, and (c) the linear tensile coefficient q_{1n}. Trailing numbers -1, -2, and -3 correspond to the low, medium, and high impact velocity simulations, 1S-1523, 2S-593, and 69ts-12-17, respectively.

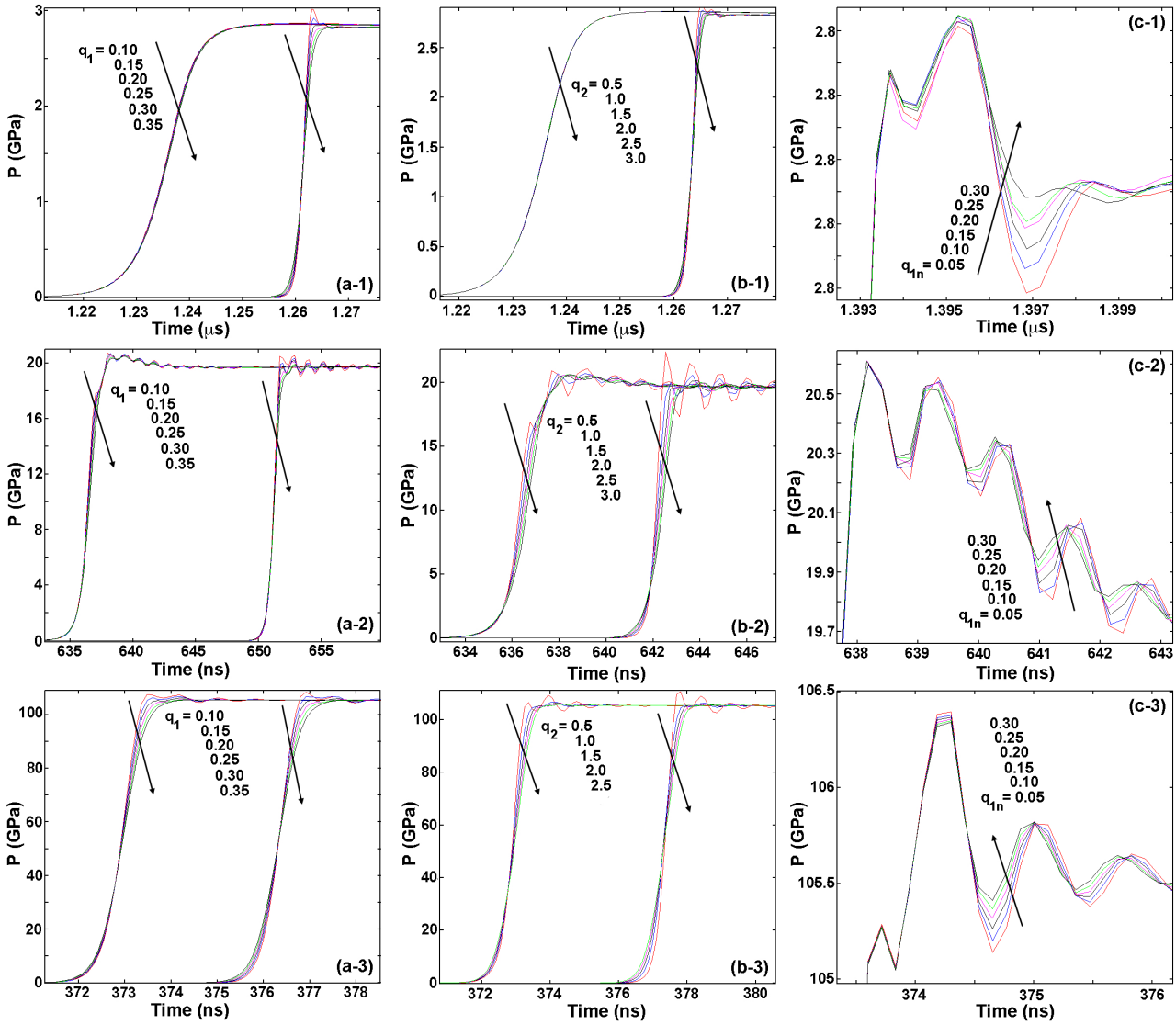

Figure 8: Effect of varying artificial viscosity parameters on the window materials illustrating pressure profiles for tracer particles located one element away from the Powder-WIndow interface and after propagating 0.5 mm into the window. Varied parameters are (a) the linear compression coefficient q_1, (b) the quadratic compression coefficient q_2, and (c) the linear tensile coefficient q_{1n}. Trailing numbers -1, -2, and -3 correspond to the low, medium, and high impact velocity simulations, 1S-1523, 2S-593, and 69ts-12-17, respectively.

For the results shown thus far, all were generated with a uniform mesh applied to the length of the problem. However, a small amount of numerical instability is still observed immediately following the rise to peak pressure in the input and propagated traces using the optimized artificial viscosity parameters defined previously, see Fig. 9(a). To determine whether or not these instabilities could be reduced via the "impedance matching" technique, a new series of simulations were run where the element thickness for the CeO_2 powder was kept constant at 5 μm, and the elements in the Cu impactor and baseplate was reduced to 2.5 μm, nominally satisfying Eq. (6). Results from the "impedance matched" problem are shown in Fig. 9(b). Inspection of the pressure profiles for the uniform mesh and the "impedance matched" mesh appear identical, such that impedance matching the Cu-Powder interface had no effect on the numerical stability of the resultant pressure profiles. Therefore, a uniform mesh of 5 μm was used in all subsequent calculations.

4.5 Parameterizing P-α

Prior to performing the suite of simulations, the exponential form of the P-α model given by Eq. (2) had to be parameterized using the three distinct definitions for $\alpha(P)$ given by Eqns. (3), (4), and (5). This was accomplished by determining the appropriate values of $\alpha(P)$ for all experiments in the compaction regime. Plotting the experimental data with the solid response for EOS 96170 and 96171 in the $P-V$ plane, as shown in Fig. 10(a), allowed one to assign all experiments with $P < 24$ GPa to the compaction regime. As a result, only experiments 56-11-20, 56-11-19, 56-11-56, 1S-1525, 56-12-01, 56-12-13, 56-12-06, 56-11-26, 56-11-27, 56-11-55, 1S-1523, and 2S-589 were used in parameterizing the various forms of $\alpha(P)$, see Table 1. Furthermore, inspection of Fig. 10 reveals that in the regime where compaction occurs EOS 96170 and 96171 overlap, such that parameterization of the P-α models needs only to be considered with respect to the low pressure phase, i.e. 96170. All parameterizations for $\alpha(P)$ were made with the average initial sample density of $\rho_{00} = 4.03$ g/cm^3.

4.5.1 $\alpha_1 = V/V_0$

For the case where $\alpha_1 = V/V_0$, Eq. (3), parameterizing the P-α model was relatively straightforward. Here, the experimentally determined volume at pressure for a given experiment, see Table 1, was divided directly by the reference crystal volume, $V_0 = 0.1386$ cm^3/g. The corresponding $\alpha(P)$ values were then fit with a two-term exponential form of Eq. (2), resulting in the following fitting parameters: $a_1 = 0.3564$, $a_2 = 0.4361$, $b_1 = 152.1$, and $b_2 = 29.22$, where pressure is in Mbar^{-1} and the root mean square error was $R^2 > 0.99$. The calculated P-α crush response for this fit is shown as curve **5** in Fig. 10(b) and (c). Note that $\alpha \to 1$ as the pressure approaches ~12 GPa, and at this point the P-V response becomes vertical at $V = 0.1386$. This indicates that at $P > 12$ GPa the material has fully solidified and should follow along the porous EOS.

4.5.2 $\alpha_2 = V/V_{SS}$

With both 96170 and 96171 overlapping in the compaction region, the solid response $V_{SS}(P)$ could be adequately modeled using either EOS, and in the current investigation 96170 was chosen to represent the response of the solid. To adequately determine $V_{SS}(P)$ tabular P-V data was generated for solid 96170 using OpenSESAME, and was fit to determine C_0 the ambient sound speed and S the slope in the linear relation $U_S = C_0 + Su_P$. Inherent in this approximation is that the U_S-u_P Hugoniot response of the solid cubic fluorite phase can be adequately described using the linear approximation. The resultant parameters fit for the solid material were $C_0 = 5.725$ km/s and $S = 1.454$ with an $R^2 = 1$. Using these parameters one can solve directly for $V_{SS}(P)$ with the Hugoniot jump conditions to arrive at:[1]

$$V_{SS}(P) = \frac{S-1}{S}V_0 + \frac{C_0^2}{2S^2P}\left[-1+\left(1+\frac{4SPV_0}{C_0^2}\right)^{1/2}\right]. \tag{7}$$

Values for $\alpha_2 = V/V_{SS}$ were determined by taking the experimental pressures reported in Table 1 and inserting them in to Eq. (7) to determine $V_{SS}(P)$.

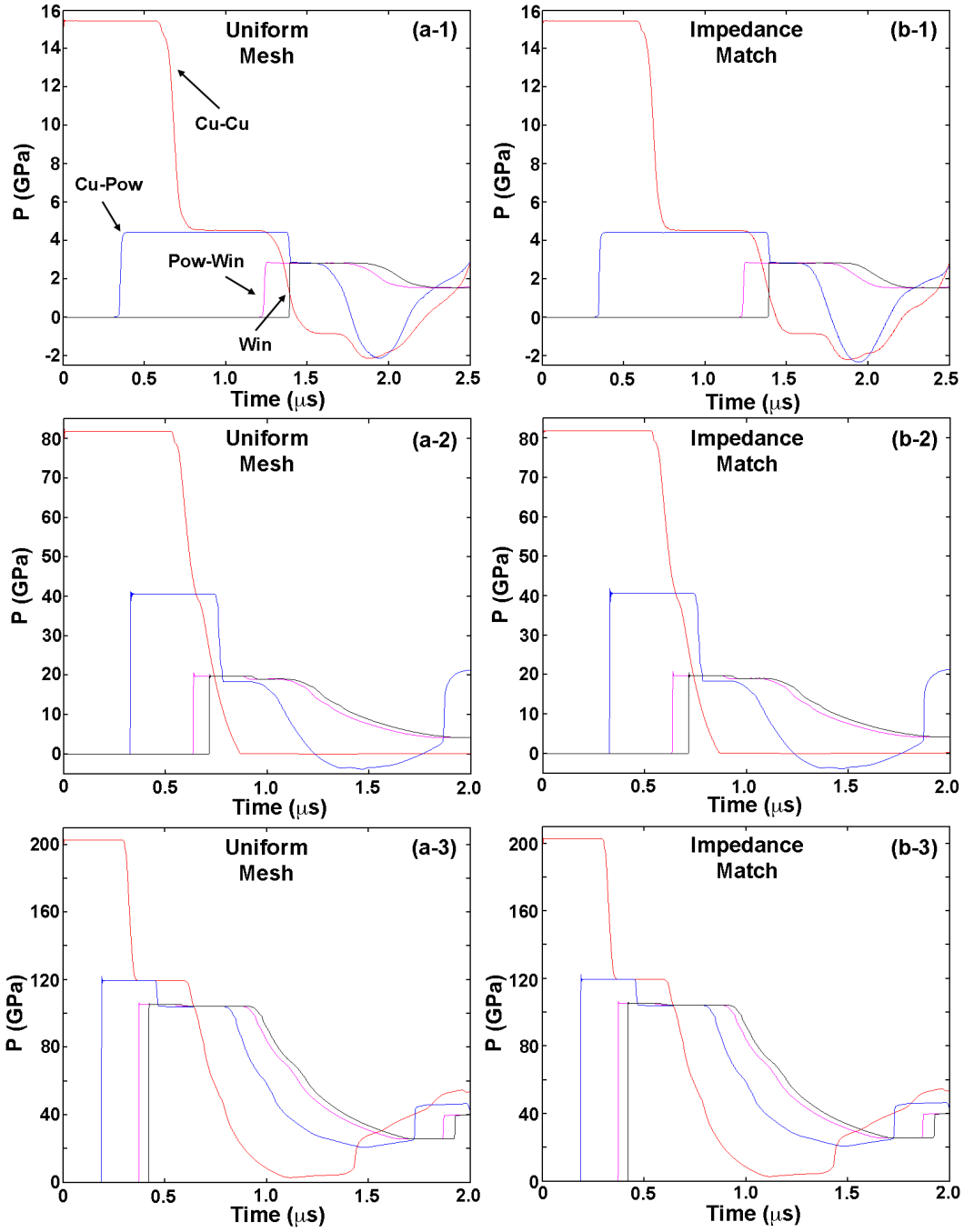

Figure 9: Effect of changing mesh zoning from (a) uniform to (b) "impedance matched" with mesh size in Cu of 2.5 μm and in CeO_2 powder of 5 μm. Trailing numbers -1, -2, and -3 correspond to the low, medium, and high impact velocity simulations, 1S-1523, 2S-593, and 69ts-12-17, respectively. Labels in (a-1) correspond to tracer locations, and are common for all images in the figure.

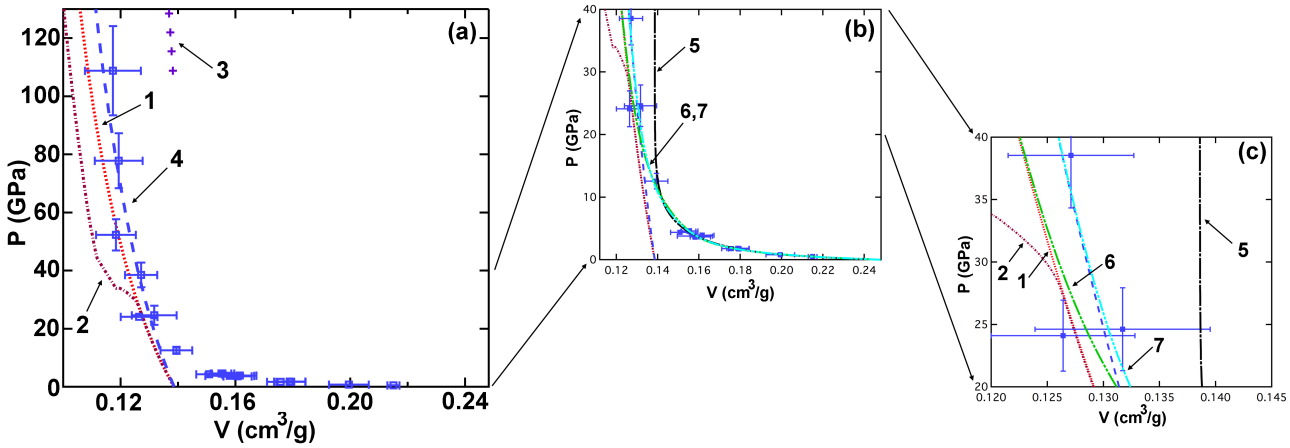

Figure 10: Graphical representation of (a) P-V response for experimentally obtained data for CeO_2 (squares), and calculated EOS response for (1) solid-liquid 96170, (2) three-phase 96171, (3) initially porous 96170 at $\rho_{00} = 4.03$ g/cm^3, and (4) porous Hugoniot fit to experimental data with $P > 24$ GPa using Mie-Grüneisen relation, Eq. (7). Also shown are zoomed in images (b) and (c), which illustrate the different P-α responses given by Eqns. (3)-(5).

The corresponding $\alpha(P)$ values were then fit with a two-term exponential form of Eq. 2, resulting in the following fitting parameters: $a_1 = 0.2592$, $a_2 = 0.5283$, $b_1 = 13.89$, and $b_2 = 104.0$. As previously, pressure is in Mbar^{-1} and $R^2 > 0.99$. The calculated crush response is shown by curve **6** in Fig. 10(b) and (c). Note that for this definition of $\alpha(P)$ the material does not asymptote to the solid EOS until ~35 GPa, see Fig. 10(c), indicating the material remains in an off-Hugoniot state at significantly higher pressures than the previous definition of alpha where $\alpha_1 = V/V_0$.

4.5.3 $\alpha_3 = V/V_{SP}$

The final definition of $\alpha(P)$ requires knowledge of the the P-V Hugoniot for the porous material, $V_{SP}(P)$, assuming the initial porosity is crushed out at any pressure $P > 0$. Ideally, one desires to determine this Hugoniot in the compaction regime from the solid EOS. However, plotting the results of OpenSESAME for EOS 96170 at an initial density of 4.03 g/cm^3 results in curve **3** in Fig. 10(a). For the relatively modest initial density sample, ~55 percent of the crystal density, the OpenSESAME solver is unable to calculate the Hugoniot response in the crush-up regime for any $P < 104$ GPa. Furthermore, inspection of Fig. 10(a) reveals that the predicted Hugoniot given by curve **3** deviates substantially from the experimentally measured response at high-pressures, thereby questioning the validity of its use in determining $\alpha(P)$ in the crush regime.

In an attempt to obtain a more realistic definition of $V_{SP}(P)$, the experimental data for $P > 24$ GPa was fit using the Mie-Grüneisen EOS with the C_0 and S parameters determined for the ambient phase solid in the previous section. In this approach it is assumed that the material remains in the cubic fluorite structure at all pressures, and that the Grüneisent gamma varies as $\gamma = V(\gamma_0/V_0)$. The pressure as a function of volume along the porous Hugoniot is defined by:

$$P = \frac{[2V_{SP} - \gamma(V_0 - V_{SP})]C_0^2(V_0 - V_{SP})}{[2V_{SP} - \gamma(V_{00} - V_{SP})][V_0 - S(V_0 - V_{SP})]^2}, \quad (8)$$

which was fit to the experimental data and resulted

in a best-fit value of $\gamma_0 = 0.6976$ with an $R^2 = 0.81$. The relatively low R^2 is a direct result of scatter in the experimental data that may be indicative of a shock-induced phase change, such that the single phase Mie-Grüneisen approach may be an oversimplification of the physics that are occurring at high-pressures. However, for lack of a more physical representation of the data in the crush regime at intermediate pressures, this approach was used because it allowed for the porous Hugoniot to be captured by a discreet and functional relationship, Eq. (8). Using the best-fit value of γ_0 in Eq. (8) the pressure along the porous Hugoniot corresponding to a given experiment in the compacting regime was determined to calculate $\alpha_3 = V/V_{SP}$. Values of $\alpha(P)$ were then fit to the two-term exponential form of Eq. (2), resulting in the fitting parameters: $a_1 = 0.4819$, $a_2 = 0.3073$, $b_1 = 114.5$, and $b_2 = 18.41$ with $R^2 > 0.99$ and pressure in Mbar^{-1}. Inspection of Fig. 10(c) indicates that $\alpha \rightarrow 1$ between 25 - 30 GPa, indicating the material remains off the porous Hugoniot at pressures intermediate to the previous two definitions of $\alpha(P)$. Tabular results for all definitions of $\alpha(P)$ are given in Table 3.

Table 3: Summary of fitting parameters for two-term exponential form of the P-α model given by $\alpha(P) = 1 + a_1\exp(-b_1 P) + a_2\exp(-b_2 P)$.

$\alpha(P) =$	a_1	a_2	b_1 (Mbar^{-1})	b_2 (Mbar^{-1})
V/V_0	0.3564	0.4361	152.1	29.22
V/V_{SS}	0.2592	0.5283	13.89	104.0
V/V_{SP}	0.4819	0.3073	114.5	18.41

5 Simulated Hugoniots

Having defined the appropriate functional forms of $\alpha(P)$ given by Eqns. (3)-(5), simulations are performed employing each variant of $\alpha(P)$ on both equations of state, 96170 and 96171. One-dimensional simulations corresponding to the series of parallel plate impact experiments whose results were given in Table 1 and whose configuration was shown in Fig. 4 were carried out for CeO_2. Nominal initial density for the CeO_2 was prescribed at 4.03 g/cm^3, the average from experiments.

Simulated one-dimensional geometries tried to reflect, as closely as possible, the average thickness values for the impactor, baseplate, powder, buffer (if used), and window from the experimental geometries. The 8 μm Al foil located at the interface between the powder and the window (or buffer) was not modeled explicitly due to the uniform mesh resolution being set at 5 μm. Validation of the EOS and combined P-α compaction models were carried out by placing tracer particles at several locations in the powder and window, and comparing simulated results with those from experiments. Specifically, comparison was made between the experimental and calculated values for the Hugoniot state and the propagated wave profiles captured with optical velocimetry (PDV[26] and VISAR[27]).

With the exception of the calculated shock velocity, which was taken from the time of flight difference between two tracer particles located one element from the impact and rear surfaces of the simulated powder material at 50% of the equilibrated peak stress (see Sec. 4.2), all simulated Hugoniot parameters were obtained directly from the tracer output at the impact surface of the powder, i.e. at the Cu-Powder interface. Simulated velocimetry profiles were recorded within the window material, as they would be in the experiment, one element from the Powder-Window interface, and at the appropriate thickness into the window to account for the buffer if one was used. It should be noted that in using the average thickness of the powder samples, jump-off of the propagated wave profiles is not expected to correspond exactly between the simulation and experiment for all cases. This is due to variations in the powder thickness that were measured experimentally at the different probe locations, and from bowing in the baseplate that occurred during initial pressing of the powder.[2] Furthermore, all simulations were performed using the average initial density of the samples from experiments, 4.03 g/cm^3, and as a result additional variation between the simulated and experimental Hugoniot states may be expected. However, variations in the Hugoniot state as a result of small fluctuations in the initial

sample density are expected to be small.[2]

5.1 Solid-Liquid EOS, 96170

The first series of simulations were run exclusively with the solid-liquid SESAME EOS 96170 to determine the effect of varying the definition of $\alpha(P)$ on the compaction and equation of state response. Comparison of the simulated and experimental Hugoniot results are given in Table 4 and plotted in Fig. 11. Generally, the simulated results tend to agree well with experiments in the compaction regime at low shock pressures and velocities, while deviating further from the measured response at higher pressures. The broad agreement at low pressures indicates that the general form of the compaction models chosen can adequately represent the consolidation processes that occur during the shock loading of CeO_2 powders. However, the rather substantial deviations observed at higher pressures may indicate the presence of a shock induced transformation that is not captured by the solid-liquid equation of state, e.g. that porous CeO_2 may undergo a shock-induced structural or stoichiometric transition. A detailed examination of the results from simulations performed with EOS 96170 is given in the sections that follow.

5.1.1 Low-Pressure Response

The low-pressure response as discussed in this section refers to all simulations and experiments where pressures in the CeO_2 powders were less than 24 GPa. These are the same experiments used in parameterizing the P-α models, see Sect. 4.5, and whose results are illustrated in Fig. 11(b) and (d). For experiments/simulations whose shock pressures were less than ∼2.0 GPa, simulated results for the shock velocities often fell outside of the experimental uncertainties, see the blue and red text in Table 4. However, in these instances the measured uncertainties were less than 0.01 km/s such that the calculated values were still within 1 - 3 % of the measured results. In the pressure range 2 - 5 GPa there continues to be generally good agreement between calculations and experiment. As a consequence, the calculated and measured results for all instances of $\alpha(P)$ where $P \leq$ 5 GPa are nearly indistinguishable from one another when plotted together in Fig. 11(b) and (d).

As pressures approach those required to reach full compaction, ∼12.5 GPa, a clear distinction between the three definitions for $\alpha(P)$ is observed, reflecting divergence of the three models with increasing pressures, see Fig. 10. Inspection of Fig. 11(b) reveals that both $\alpha_1 = V/V_0$ and $\alpha_3 = V/V_{SP}$ fall within the experimental uncertainty reported for experiment 2S-589, while $\alpha_2 = V/V_{SS}$ does not. Furthermore, between α_1 and α_3, the best agreement is obtained with α_1. This finding is somewhat surprising as the true definition for $\alpha(P)$ as defined and implemented in the code is that given by α_3. It may be that the assumptions used in defining the porous Hugoniot on which the definition for α_3 is based, as given in Sec. 4.5.3, are flawed. Recall the porous Hugoniot was obtained by fitting the experimental data with $P \geq 24$ GPa to a standard Mie-Grüneisen model, with γ_0 being the variable parameter. The relatively poor fit obtained by this method ($R^2 = 0.81$) suggests this approach may not be well suited to defining the porous Hugoniot on which α_3 should be based. However, in the absence of an alternative approach, the current methodology for defining the porous Hugoniot still results in a calculated Hugoniot that falls within the limits of experimental uncertainty for all shots within the compaction regime. In contrast, if the reference curve of the initially solid material is used to define $\alpha(P)$, as was done for α_2, there is a clear divergence between the calculated and experimental results at pressures near those required to reach solid density, see Fig. 11(b).

5.1.2 High-Pressure Response

The divergence in the calculated results near the solid density as a consequence of the varying definitions for $\alpha(P)$ does not continue as pressure is increased. Inspection of both the P-V and U_S-u_P plots in Fig. 11(a) and (c) shows that all three definitions for $\alpha(P)$ predict nominally the same response at elevated pressures. Thus, in terms of the calculated Hugoniot for instances where the the material has been shocked past the solid density, $P \geq 24$ GPa, there is no difference in the calculated response due to

Table 4: Comparison of experimental results with simulated results using SESAME EOS 96170 with definitions for $\alpha(P)$ given by Eqns. (3) - (5). Simulated results falling outside of experimental uncertainties are indicated by red and blue text, where red text indicates the simulated values lie above the upper uncertainty limit and blue text indicates values lie below the lower uncertainty limit.

Shot (#)	P (GPa)	u_P (km/s)	U_S (km/s)	ρ (g/cm^3)	Shot (#)	P (GPa)	u_P (km/s)	U_S (km/s)	ρ (g/cm^3)
56-11-20					56-11-27				
Exp.	0.80 ±.04	0.20 ±.00	1.01 ±.00	5.01 ±.17	Exp.	1.78 ±.08	0.36 ±.00	1.23 ±.01	5.69 ±.15
Sim. - α_1	0.80	0.20	1.02	4.99	Sim. - α_1	1.77	0.35	1.24	5.64
Sim. - α_2	0.82	0.20	1.05	4.96	Sim. - α_2	1.78	0.35	1.24	5.63
Sim. - α_3	0.81	0.20	1.04	4.97	Sim. - α_1	1.78	0.35	1.24	5.63
56-11-19					56-11-55				
Exp.	1.82 ±0.17	0.36 ±.00	1.27 ±.00	5.59 ±.17	Exp.	3.67 ±.26	0.57 ±.01	1.61 ±.07	6.22 ±.19
Sim. - α_1	1.79	0.36	1.24	5.65	Sim. - α_1	3.62	0.57	1.58	6.28
Sim. - α_2	1.79	0.36	1.25	5.63	Sim. - α_2	3.69	0.57	1.61	6.20
Sim. - α_3	1.79	0.36	1.25	5.64	Sim. - α_3	3.67	0.57	1.61	6.22
56-11-56					1S-1523				
Exp.	3.92 ±.24	0.58 ±.01	1.67 ±.09	6.19 ±.22	Exp.	4.57 ±.35	0.65 ±.02	1.75 ±.03	6.43 ±.17
Sim. - α_1	3.79	0.58	1.61	6.33	Sim. - α_1	4.47	0.65	1.71	6.46
Sim. - α_2	3.86	0.58	1.65	6.24	Sim. - α_2	4.58	0.64	1.77	6.37
Sim. - α_3	3.84	0.58	1.64	6.26	Sim. - α_3	4.56	0.65	1.75	6.34
1S-1525					2S-589				
Exp.	4.59 ±.24	0.66 ±.01	1.74 ±.05	6.45 ±.14	Exp.	12.6 ±1.2	1.17 ±.03	2.67 ±.06	7.18 ±.29
Sim. - α_1	4.57	0.66	1.73	6.47	Sim. - α_1	12.6	1.17	2.68	7.06
Sim. - α_2	4.69	0.65	1.78	6.34	Sim. - α_2	12.9	1.16	2.76	6.87
Sim. - α_3	4.66	0.65	1.77	6.37	Sim. - α_3	12.8	1.16	2.73	6.95
56-12-01					2S-594				
Exp.	1.72 ±.18	0.35 ±.01	1.24 ±.00	5.59 ±.16	Exp.	24.6 ±3.3	1.72 ±.05	3.61 ±.26	7.59 ±.45
Sim. - α_1	1.71	0.35	1.22	5.61	Sim. - α_1	26.0	1.69	3.83	7.13
Sim. - α_2	1.71	0.35	1.23	5.59	Sim. - α_2	26.1	1.69	3.85	7.09
Sim. - α_3	1.71	0.35	1.23	5.60	Sim. - α_3	26.1	1.69	3.84	7.11
56-12-13					2S-593				
Exp.	3.78 ±.48	0.59 ±.01	1.60 ±.14	6.33 ±.34	Exp.	38.6 ±4.2	2.16 ±.05	4.43 ±.23	7.87 ±.35
Sim. - α_1	3.80	0.59	1.61	6.32	Sim. - α_1	40.9	2.11	4.80	7.08
Sim. - α_2	3.87	0.58	1.65	6.23	Sim. - α_2	40.9	2.11	4.80	7.07
Sim. - α_3	3.85	0.58	1.64	6.25	Sim. - α_3	40.9	2.11	4.80	7.08
56-12-06					69ts-12-09				
Exp.	4.37 ±.28	0.65 ±.01	1.66 ±.07	6.63 ±.20	Exp.	52.3 ±5.4	2.61 ±.05	4.98 ±.31	8.45 ±.49
Sim. - α_1	4.46	0.66	1.71	6.46	Sim. - α_1	58.4	2.51	5.79	7.06
Sim. - α_2	4.57	0.64	1.76	6.33	Sim. - α_2	58.4	2.51	5.79	7.06
Sim. - α_3	4.54	0.64	1.75	6.37	Sim. - α_3	58.4	2.51	5.79	7.06
2S-648					69ts-12-23				
Exp.	24.11 ±.29	1.71 ±.04	3.49 ±.23	7.91 ±.40	Exp.	77.8 ±9.4	3.14 ±.07	6.10 ±.42	8.38 ±.59
Sim. - α_1	25.68	1.68	3.79	7.13	Sim. - α_1	84.8	3.04	6.92	7.15
Sim. - α_2	25.79	1.67	3.82	7.09	Sim. - α_2	84.8	3.04	6.92	7.15
Sim. - α_3	25.72	1.68	3.80	7.11	Sim. - α_3	84.8	3.04	6.92	7.15
56-11-26					69ts-12-17				
Exp.	0.51 ±.03	0.13 ±.00	0.97 ±.03	4.65 ±.05	Exp.	109 ±15	3.79 ±.09	7.16 ±.60	8.53 ±.71
Sim. - α_1	0.50	0.13	0.95	4.69	Sim. - α_1	120	3.65	8.14	7.28
Sim. - α_2	0.52	0.13	0.99	4.66	Sim. - α_2	120	3.65	8.14	7.27
Sim. - α_3	0.51	0.13	0.98	4.67	Sim. - α_3	120	3.65	8.14	7.27

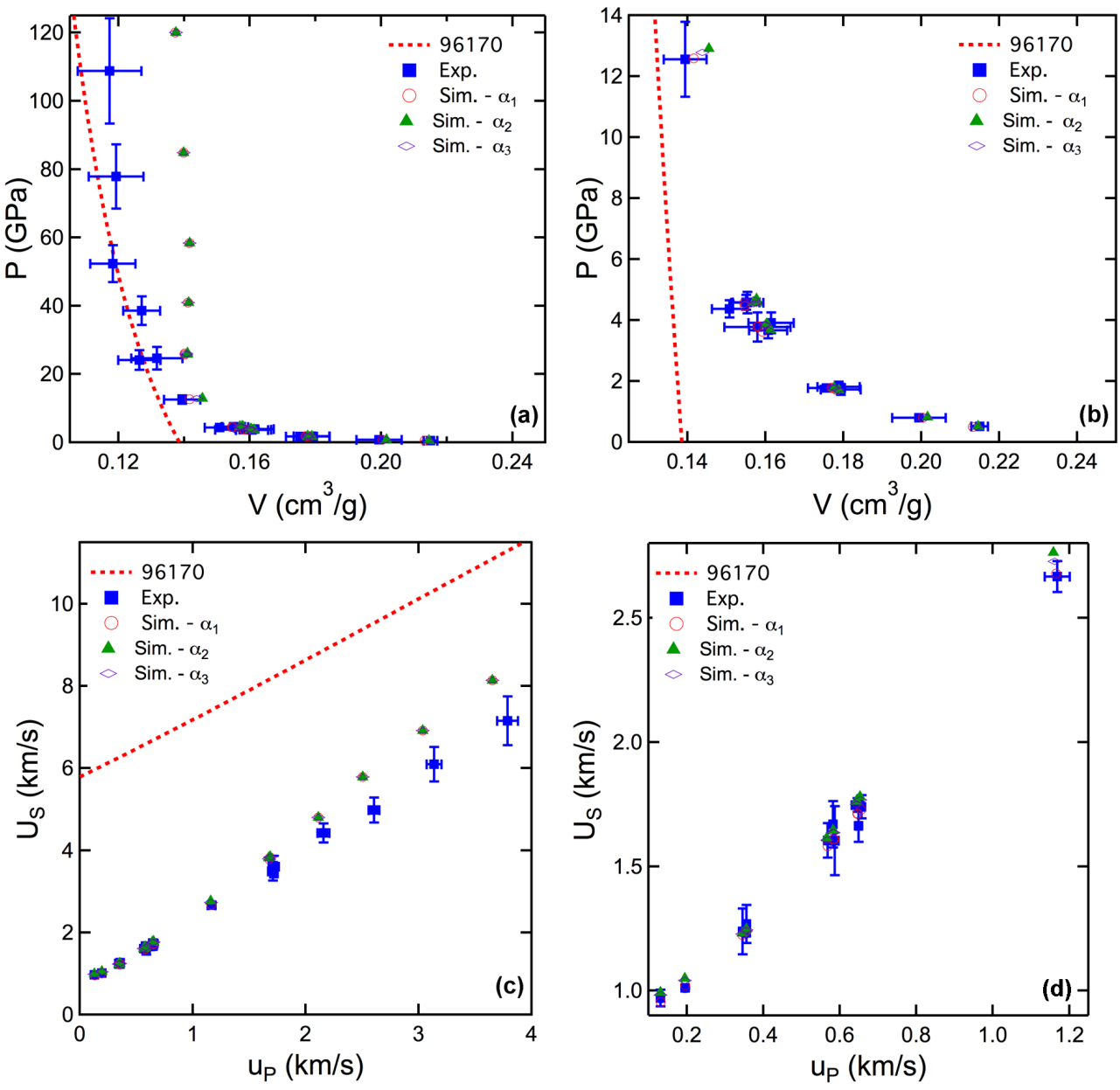

Figure 11: Hugoniot results for SESAME EOS 96170 with $\alpha = \alpha_1 = \circ$, $\alpha_2 = \blacktriangle$, $\alpha_3 = \diamond$ plotted with experimental results ■ and calculated solid response (dashed line)

the definition of $\alpha(P)$ for the solid-liquid EOS 96170. However, the simulated response is markedly different from what is measured experimentally.

An examination of the calculated results with those obtained from experiments in the range $P \geq 24$ GPa finds that rather significant deviations, which tend to increase with increasing magnitude of the shocked state, are observed, see Fig. 11(a) and (c). Experimentally, data in the P-V plane appears to compress further as pressure is increased from ∼24 - 52 GPa, prior to asymptoting to a nearly linear response at ∼52 GPa. Computationally, the asymptotic behavior begins at ∼24 GPa, and continues to the highest pressures reached in the current study. Linearity in the P-V response indicates that the competing processes of compaction due to the applied pressure (reduction in volume) and expansion due to increasing thermal effects (increase in volume) are approximately equivalent over the given pressure range. While both experiments and simulations exhibit this behavior, the fact that linearity begins a lower pressure in the calculations suggests the possibility of an additional mechanism of compression not included in EOS 96170 is occurring experimentally in the range 24 - 52 GPa. To investigate whether this mechanism could be a shock induced polymorphic phase transition, experimental results are compared against calculations using SESAME EOS 96171, which includes the transition from cubic to orthorhombic at high pressures.

5.2 Three-Phase EOS, 96171

The next series of simulations were performed with the three-phase SESAME EOS 96171, which explicitly includes the shock-induced cubic to orthorhombic phase change. In a manner consistent with the previous set of simulations, each of the three definitions for $\alpha(P)$ were tested to determine its effect on the calculated Hugoniot state. However, it is expected that in the compaction regime results from 96171 and 96170 will be very similar because of the chosen definitions for $\alpha(P)$. For the case of α_1, $\alpha(P)$ is based solely in the initial solid density and does not take into account a specific SESAME EOS. For α_2, $\alpha(P)$ considers only the behavior of the solid, which in the compaction regime is still in its ambient cubic crystal structure. Lastly, for α_3, $\alpha(P)$ is determined using only the high-pressure experimental data in the manner outlined in Sec. 4.5.3, and as such also does not take into account any specific EOS. Results from these simulations are given in Table 5 and plotted alongside experimental results in Fig. 12, where inspection of Fig. 12 clearly illustrates the presence of the high-pressure phase change in both the P-V and U_S-u_P calculated solid response.

5.2.1 Low-Pressure Response

As postulated, the calculated low-pressure response (<24 GPa) for the three-phase EOS is consistent with that predicted using the solid-liquid EOS. Specifically, agreement between EOS calculations in this range is typically better than 1% with several instances falling within the 1-2% range. The observed variance does not tend to exhibit any noticeable trends with respect to the definition of $\alpha(P)$. As a consequence, the low pressure results for the three-phase EOS, when plotted, look nearly identical to those for the solid-liquid EOS given in Fig. 11(b) and (d). Therefore the comments made in Sec. 5.1.1 for the solid-liquid EOS also apply to the compaction regime for the three-phase EOS.

At pressures less <5 GPa all variants for the definition of $\alpha(P)$ are nearly indistinguishable from the experiment data, and at the slightly elevated pressure of ∼12.5 GPa α_1, which is based on the initial solid density, comes the closest to matching the experimental results. These findings suggest that for a material whose solid response does not undergo a phase change at pressures below which full compaction is expected to occur, the compaction responses predicted by a solid-liquid or three-phase EOS are comparable. This permits calculations to be performed in the compaction regime with either EOS. However, the same can not be said of the higher pressure regime, where distinct differences are observed between the two EOS.

5.2.2 High-Pressure Response

As shock pressures are increased, the three-phase EOS 96171 achieves better agreement with experi-

Table 5: Comparison of experimental results with simulated results using SESAME EOS 96171 with definitions for α given by Eqns. (3) - (5). Simulated results falling outside of experimental uncertainties are indicated by red and blue text, where red text indicates the simulated values lie above the upper uncertainty limit and blue text indicates values lie below the lower uncertainty limit.

Shot (#)	P (GPa)	u_P (km/s)	U_S (km/s)	ρ (g/cm^3)	Shot (#)	P (GPa)	u_P (km/s)	U_S (km/s)	ρ (g/cm^3)
56-11-20					56-11-27				
Exp.	0.80 ±.04	0.20 ±.00	1.01 ±.00	5.01 ±.17	Exp.	1.78 ±.08	0.36 ±.00	1.23 ±.01	5.69 ±.15
Sim. - α_1	0.80	0.20	1.02	4.99	Sim. - α_1	1.78	0.35	1.24	5.64
Sim. - α_2	0.82	0.20	1.05	4.96	Sim. - α_2	1.78	0.35	1.24	5.63
Sim. - α_3	0.81	0.20	1.04	4.97	Sim. - α_1	1.78	0.35	1.24	5.63
56-11-19					56-11-55				
Exp.	1.82 ±0.17	0.36 ±.00	1.27 ±.00	5.59 ±.17	Exp.	3.67 ±.26	0.57 ±.01	1.61 ±.07	6.22 ±.19
Sim. - α_1	1.79	0.36	1.24	5.65	Sim. - α_1	3.63	0.57	1.58	6.28
Sim. - α_2	1.79	0.36	1.25	5.64	Sim. - α_2	3.69	0.57	1.61	6.20
Sim. - α_3	1.79	0.36	1.24	5.64	Sim. - α_3	3.67	0.57	1.61	6.22
56-11-56					1S-1523				
Exp.	3.92 ±.24	0.58 ±.01	1.67 ±.09	6.19 ±.22	Exp.	4.57 ±.35	0.65 ±.02	1.75 ±.03	6.43 ±.17
Sim. - α_1	3.79	0.58	1.61	6.33	Sim. - α_1	4.47	0.65	1.71	6.46
Sim. - α_2	3.86	0.58	1.65	6.24	Sim. - α_2	4.58	0.64	1.76	6.33
Sim. - α_3	3.85	0.58	1.64	6.26	Sim. - α_3	4.56	0.65	1.75	6.37
1S-1525					2S-589				
Exp.	4.59 ±.24	0.66 ±.01	1.74 ±.05	6.45 ±.14	Exp.	12.6 ±1.2	1.17 ±.03	2.67 ±.06	7.18 ±.29
Sim. - α_1	4.57	0.66	1.73	6.47	Sim. - α_1	12.6	1.17	2.68	7.04
Sim. - α_2	4.70	0.65	1.78	6.34	Sim. - α_2	12.9	1.16	2.77	6.85
Sim. - α_3	4.66	0.65	1.77	6.37	Sim. - α_3	12.8	1.16	2.73	6.93
56-12-01					2S-594				
Exp.	1.72 ±.18	0.35 ±.01	1.24 ±.00	5.59 ±.16	Exp.	24.6 ±3.3	1.72 ±.05	3.61 ±.26	7.59 ±.45
Sim. - α_1	1.71	0.35	1.22	5.61	Sim. - α_1	24.5	1.72	3.59	7.86
Sim. - α_2	1.71	0.35	1.23	5.59	Sim. - α_2	24.5	1.72	3.61	7.79
Sim. - α_3	1.71	0.35	1.23	5.60	Sim. - α_3	24.5	1.72	3.60	7.83
56-12-13					2S-593				
Exp.	3.78 ±.48	0.59 ±.01	1.60 ±.14	6.33 ±.34	Exp.	38.6 ±4.2	2.16 ±.05	4.43 ±.23	7.87 ±.35
Sim. - α_1	3.80	0.59	1.61	6.32	Sim. - α_1	38.1	2.16	4.35	7.97
Sim. - α_2	3.88	0.58	1.65	6.23	Sim. - α_2	38.1	2.16	4.36	7.77
Sim. - α_3	3.86	0.58	1.64	6.25	Sim. - α_3	38.1	2.16	4.35	7.82
56-12-06					69ts-12-09				
Exp.	4.37 ±.28	0.65 ±.01	1.66 ±.07	6.63 ±.20	Exp.	52.3 ±5.4	2.61 ±.05	4.98 ±.31	8.45 ±.49
Sim. - α_1	4.46	0.65	1.71	6.46	Sim. - α_1	54.1	2.57	5.21	7.90
Sim. - α_2	4.58	0.64	1.76	6.33	Sim. - α_2	54.1	2.57	5.21	7.69
Sim. - α_3	4.54	0.64	1.75	6.37	Sim. - α_3	54.1	2.57	5.21	7.69
2S-648					69ts-12-23				
Exp.	24.11 ±.29	1.71 ±.04	3.49 ±.23	7.91 ±.40	Exp.	77.8 ±9.4	3.14 ±.07	6.10 ±.42	8.38 ±.59
Sim. - α_1	24.32	1.70	3.59	7.85	Sim. - α_1	79.5	3.11	6.35	7.71
Sim. - α_2	24.32	1.70	3.61	7.79	Sim. - α_2	79.5	3.11	6.35	7.68
Sim. - α_3	24.32	1.70	3.60	7.82	Sim. - α_3	79.5	3.11	6.35	7.68
56-11-26					69ts-12-17				
Exp.	0.51 ±.03	0.13 ±.00	0.97 ±.03	4.65 ±.05	Exp.	109 ±15	3.79 ±.09	7.16 ±.60	8.53 ±.71
Sim. - α_1	0.50	0.13	0.95	4.69	Sim. - α_1	114	3.73	7.60	7.76
Sim. - α_2	0.51	0.13	1.00	4.66	Sim. - α_2	114	3.73	7.56	7.53
Sim. - α_3	0.51	0.13	0.98	4.67	Sim. - α_3	114	3.73	7.56	7.99

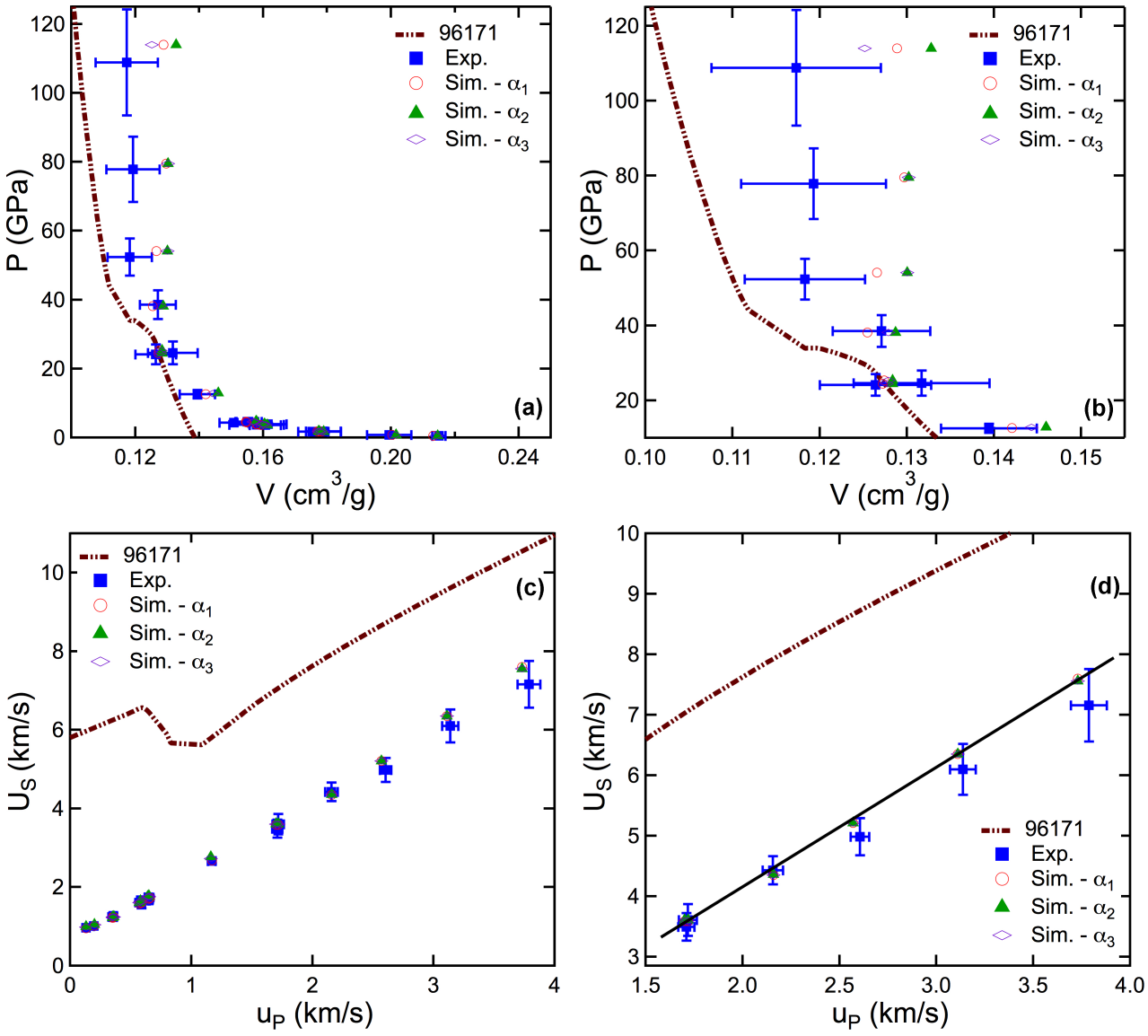

Figure 12: Hugoniot results for SESAME EOS 96171 with $\alpha = \alpha_1 = \circ$, $\alpha_2 = \blacktriangle$, $\alpha_3 = \diamond$ plotted with experimental results ■ and calculated solid response (dashed line). Solid line in (d) is a guide to the eyes to illustrate linear response of simulated results.

ment than did the solid-liquid EOS 96170. Examination of Table 5 reveals that with the exception of the calculated density for the three highest impact velocity shots (69ts-12-09, -23, -17), all calculated parameters fall within the uncertainty limits of the experiments for $P > 24$ GPa; inspection of the plots in Fig. 12 more clearly indicate this trend. In all instances in both the P-V and U_S-u_P responses, the three-phase EOS is in much better agreement with experimental data than the solid-liquid EOS (compare Fig. 11(a) and (c) to Fig. 12(a) and (c)). The improvement in agreement with implementation of EOS 96171 suggests that a shock-induced phase transformation is occurring and is measured during the timescale of the experiments, and that this transformation is at least partly responsible for the high degree of compression observed in the experimental data at elevated pressures. That the results calculated with the three-phase EOS do not match the data more exactly may indicate a need to refine the EOS at elevated pressures. It may also indicate the presence of an additional transformation and/or volume compression mechanism at elevated pressures; however, this assertion is speculative and requires further verification.

Recalling that the diamond anvil cell (DAC) data on which the three-phase EOS was calibrated reached a maximum pressure of only ∼70 GPa,[9] if an additional transformation were to exist at higher pressures, there are currently no experimental results that show this definitively. However, a closer inspection of the U_S-u_P data shown in Fig. 12(d) reveals the possibility that a higher pressure transition may exist. In Fig. 12(d) a straight line is shown that intersects the two lower pressure experiments and calculations, while also intersecting the three highest pressure computational points. Under shock loading conditions linear U_S-u_P responses are commonly observed in non-phase transitioning materials, where deviations in linearity are often interpreted as evidence of a shock-induced phase transition. Experimentally, shock velocities for the three highest pressure points deviate to lower velocities than are predicted by 96171. This suggests that there may be an additional volume reduction mechanism occurring at high-pressures that is not currently captured by the three-phase EOS.

Experimental evidence has shown that the inclusion of porosity, and the accompanying increase in temperature, can reduce the onset pressure at which certain shock-induced transformations occur.[1] If this behavior is exhibited by the CeO_2 system, the transformation from cubic to orthorhombic observed in the solid DAC samples between 30-40 GPa may actually begin at a much lower pressure for the shock compressed porous material. The same argument likely holds true for any transformation that occurs at pressures >70 GPa in solid, for which no corresponding DAC data exists. Higher pressure DAC data would help determine if any additional transformations exist at pressures >70 GPa in the solid.

Another aspect of the high-pressure response worth noting is the deviation in the calculated volumes that occurs as a result of the varying definitions for $\alpha(P)$ with application of the three-phase EOS. A similar variation is not observed for the solid-liquid EOS, where all definitions for $\alpha(P)$ converge. Inspection of Fig. 12(b), which shows the calculated and experimental P-V response between 10-125 GPa, reveals a shift in the relative volume predictions with respect to a given definition for $\alpha(P)$ with increasing pressure. At lower pressures $\alpha_1 = V/V_0$ is the closest to predicting the experimental volume, while $\alpha_2 = V/V_{SS}$ is the furthest and $\alpha_3 = V/V_{SP}$ is in the middle (see lowest pressure data points in Fig. 12(b)). However, as pressure increases to ∼50 GPa the volumes predicted by both α_2 and α_3 are the same, while that predicted by α_1 is again the closest to experiment. At ∼80 GPa the volumes predicted by all three definitions for $\alpha(P)$ converge. At sim110 GPa α_3 becomes the preferred prediction with a volume that lies closest to the experimental value, while α_1 is in the middle and α_2 is again the furthest from experiment. In an attempt to gain insight into how and why this behavior occurs, the P-α model definitions are re-examined in greater detail.

As outlined in Sec. 4.5 the P-α models given by Eqns. (3)-(5), were fit using the available experimental data below 24 GPa, resulting in the parameterization for $\alpha_i(P)$ given in Table 3. These fits, along with the lower pressure data used to parameterize them are shown Fig. 13(a). At pressures below ∼2

GPa $\alpha(P)$ for all three models is nearly identical. As pressure is increased the models diverge before re-converging at $\alpha = 1$ at ∼20-40 GPa as shown in Fig. 13(b). While the experimental data for $P > 24$ GPa was not used in parameterizing the P-α models, it is instructive to examine how the higher pressure data looks in the α-P plane. In Fig. 13(b) it is evident that depending on the definition, the experimental values of $\alpha(P)$ range from values both well above and well below its asymptotic value of one. However, the calculations are only aware of the behavior of $\alpha(P)$ defined by Eq. (2) with the parameters listed in Table 3, resulting in the dashed lines in Fig. 13(a) and (b). As such, at any pressure above that required for $\alpha(P)$ to reach one the simulated response for all three definitions for $\alpha(P)$ should be controlled solely by the EOS.

Interestingly, in contrast to the solid-liquid EOS where all definitions for $\alpha(P)$ converged to a similar response at high pressures, calculations performed with the three-phase EOS result in substantially different shock compressed volumes at high pressures. This behavior is illustrated in Fig. 12(b), and its origin is presently not known. Considering the divergence in the calculated response at high pressures, one might expect its origin to stem from the divergence in $\alpha_i(P)$ shown at lower pressures in Fig. 13, as this is the only quantitative input difference between the three sets of simulations. If this were the case, one might expect that the calculated response for α_1 to be at one extreme, while that of α_2 is at the other extreme and α_3 is in the middle, corresponding to relative positions for the three $\alpha(P)$ lines in Fig. 13. While this may be the case in the intermediate pressure range of ∼10 - 40 GPa, see Fig. 12(b), as pressure is increased the calculated results tend to converge near 80 GPa prior to α_3 achieving the extreme state of compression with relation to α_1 and α_2. It may be that the shock energy is somehow partitioned differently at high pressures due to the low pressure compaction response; however, this explanation requires further investigation.

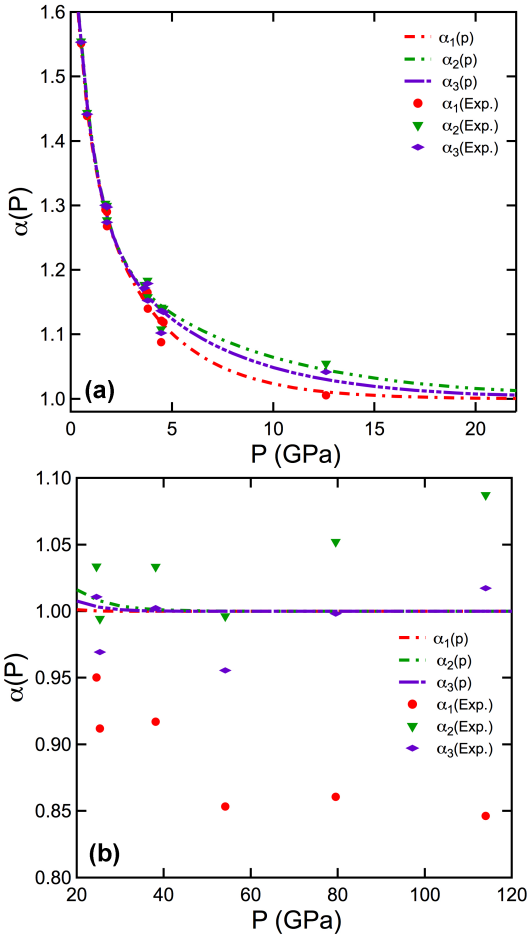

Figure 13: Plots of $\alpha(P)$ at (a) low-pressure where model is fit to data and (b) high-pressure where models asymptote to $\alpha(P) = 1$.

6 Simulated Wave-Profiles

To gain further insight into how the different compaction models effect the solid-liquid and three-phase EOS responses, velocity profiles of the simulated input and propagated waves are examined with respect to those measured in experiments. Comparisons such as these can also offer a means by which the experimental design/fixture can be analyzed with regard to true one-dimensionality of the shock state, a necessary component for a "Hugniot analysis" of the results. Simulated and experimentally obtained wave profiles are given in Figs. 14 - 17, where only the simulations corresponding to experiments performed on the rod morphology of CeO_2 are given, see Table 1. Experimental velocimetry profiles from the lower impact velocity shots, 56-11-26, -27, -55, and 1S-1523, were collected after the shock passed through a 0.5 mm thick PMMA buffer, while those for all higher impact velocity shots were collected on a foil at the powder/interface. A detailed explanation of the pertinent features observed in the simulated wave profiles is given in the paragraphs that follow.

6.1 Crush Regime

Simulations performed with either the solid-liquid (96170) or three-phase (96171) equations of state at impact velocities less than $V_I < 1.5$ km/s result in wave profiles that are nearly indistinguishable from one another for a given impact condition, such that equivalent results are obtained for CeO_2 with either the solid-liquid or three-phase EOS. This finding reveals that initially porous CeO_2 remains stable in its low-pressure cubic fluorite phase at pressures as high as $P \leq$12.6 GPa during the simulations. Inspection of the low-pressure P-V experimental results shown in Fig. 10(a) and (b) reveals the material asymptotically approaches the solid as pressure increases. That the crush response in the low-pressure regime can be fit well with a single two-term exponential, and that it does not exhibit any noticeable discontinuities supports the computational findings that CeO_2 remains in the cubic fluorite phase within the crush regime.

Another salient feature of the propagated wave profiles in the low-pressure regime is that the varying definitions for $\alpha(P)$ have very little effect on the arrival times and shape of the propagated waves. At the lowest impact velocity investigated, $V_I = 0.146$ km/s, three distinct propagated wave profiles are observed for $\alpha(P) = \alpha_1$, α_2, and α_3, where that predicted by α_1 (Eqn. (3)) is called out specifically in Fig. 14. With increasing impact velocity all three definitions for $\alpha(P)$ converge to a nearly identical wave profile at the time scales shown in Figs. 14 and 15, and reflect convergence of the three P-α definitions in the low-pressure range of Fig. 10(b). Similarity in the propagated wave profiles regardless of the chosen form of $\alpha(P)$ (within the definitions set forth in the present investigation), allows for simulations to be performed in the compaction regime equally well with any one of the three definitions for $\alpha(P)$ given by Eqns. (3)-(5). This is not to say that how one defines $\alpha(P)$ is not important. Recall that varying the definition for $\alpha(P)$ had a strong influence on the predicted behavior at high pressures when CeO_2 was modeled with the three-phase EOS (see Sec. 5.2.2).

Propagated wave profiles in the low-pressure regime also allow for assertions to be made regarding one-dimensionality of the incident wave in a given experiment to ensure correct determination of the Hugoniot state. To facilitate this type of analysis, the simulated incident waves (those transmitted into the powder from the Cu baseplate) are plotted along with the propagated profiles to help assess when the release state arrives in the one-dimensional simulation for comparison with the wave profile in the three-dimensional experiment. Again examining the lowest impact velocity experiment in Fig. 14, one can see that the peak velocity state predicted by the simulations is considerably lower than that achieved in the experiment. In this figure the release wave from the back of the impactor (at the Al/Cu interface) occurs at the impact surface of the powder nearly $\sim$750 ns prior to shock breakout at the plane of the velocimetry measurement at the buffer/window interface. Therefore, it may be that the reduced magnitude of the peak velocity state calculated for shot 56-11-26 is due to release waves traveling faster in the calculation than they do in the experiment. In addition, edge waves originating from the higher impedance stainless steel (SS) cell surrounding the

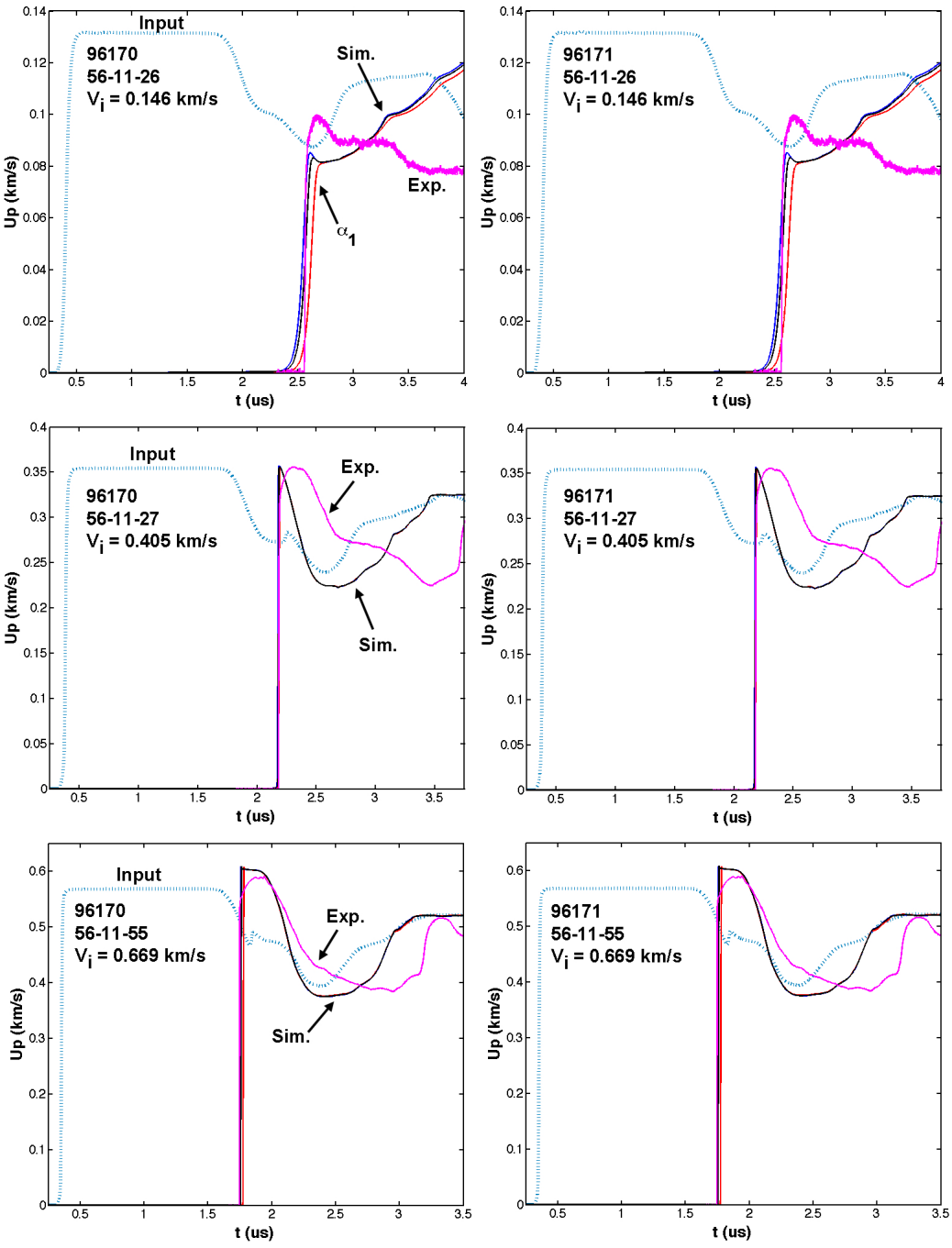

Figure 14: Material velocity wave profiles for shots 56-11-26, 56-11-27, and 56-11-55. Simulated input wave entering the powder is shown by dashed line. Propagated waves (simulated and experimental) shown by solid lines, and are marked with respect to the definitions for α_1, α_2, and α_3 where observable differences exist.

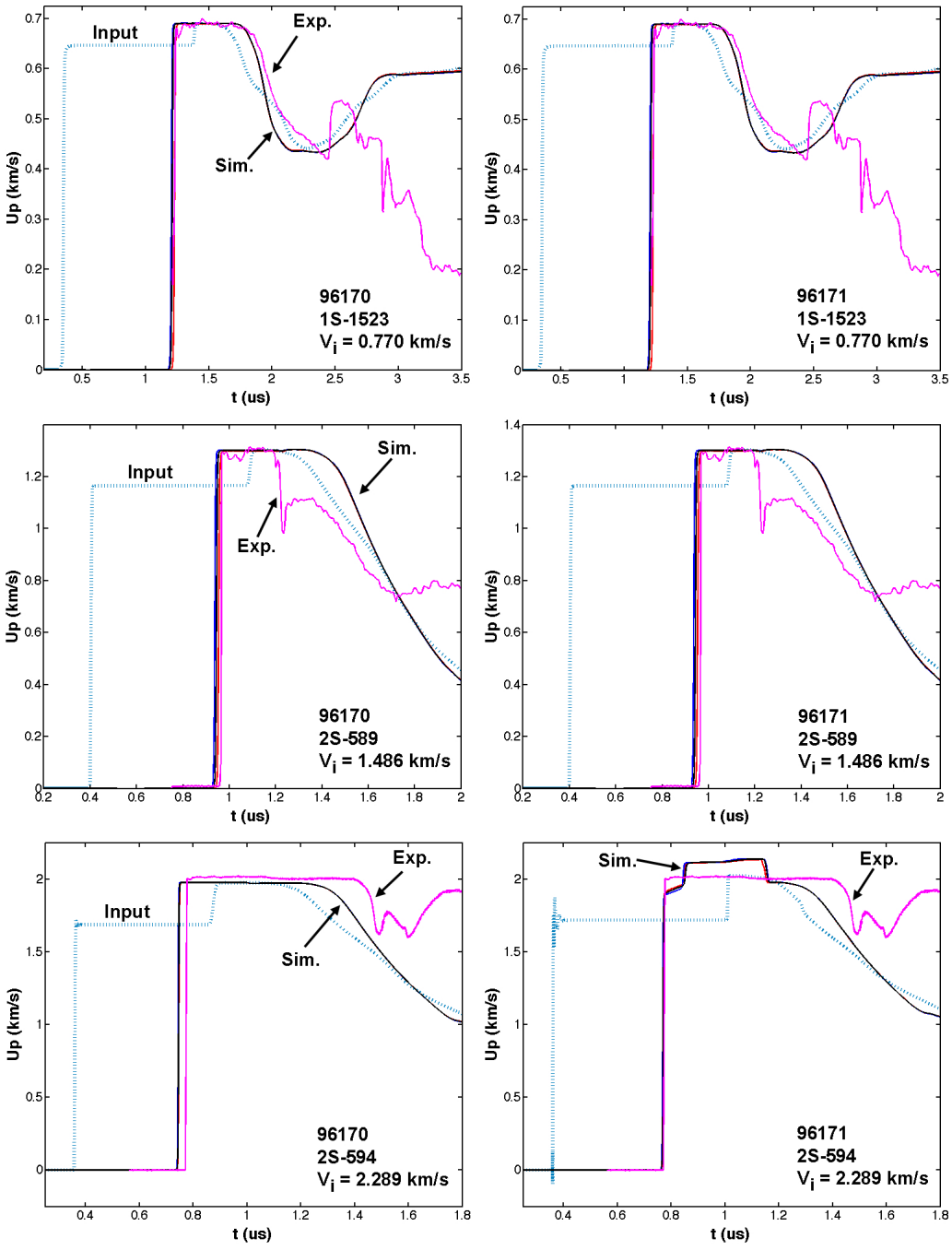

Figure 15: Material velocity wave profiles for shots 1S-1523, 2S-589, and 2S-594. Simulated input wave entering the powder is shown by dashed line. Propagated waves (simulated and experimental) shown by solid lines, and are marked with respect to the definitions for α_1, α_2, and α_3 where observable differences exist.

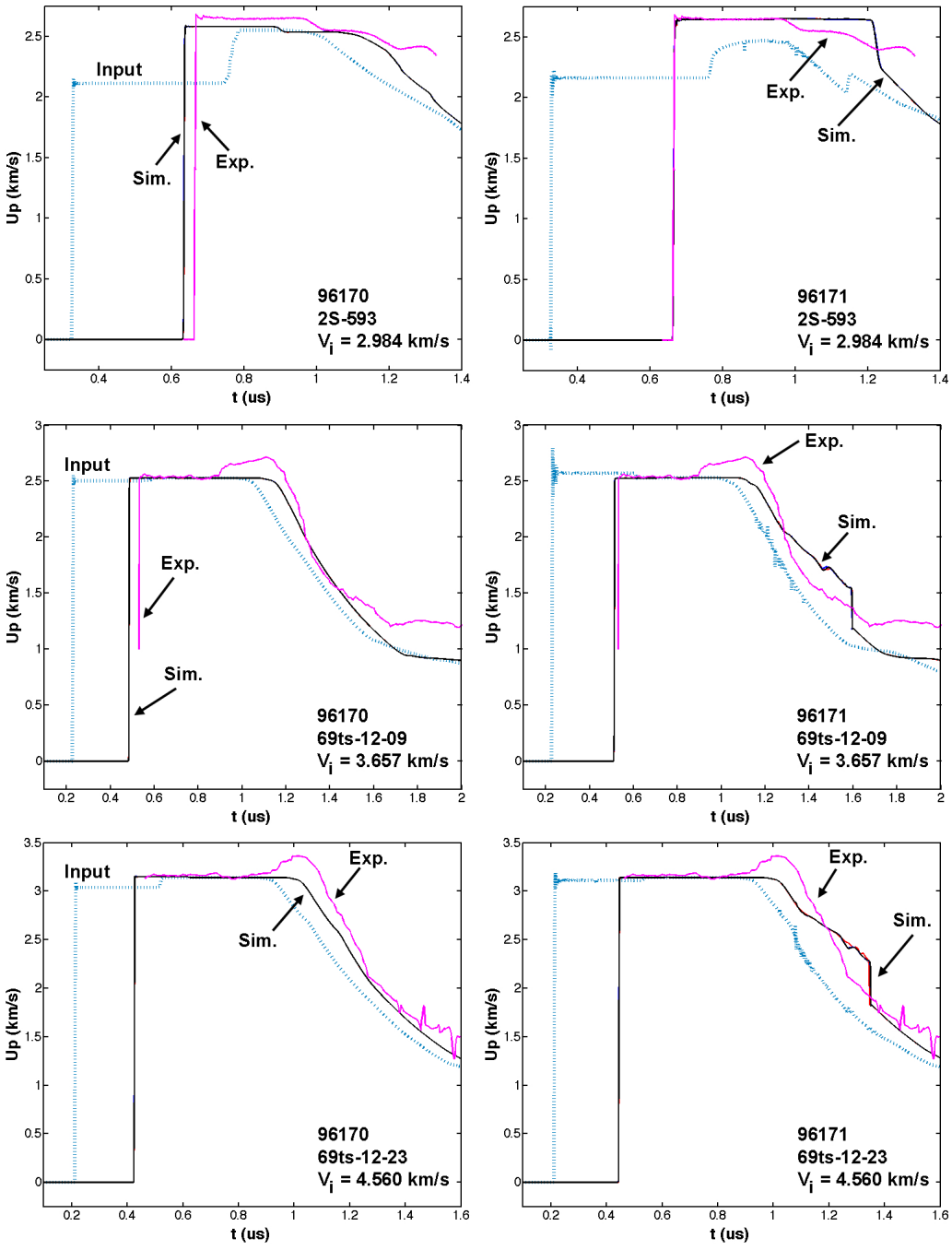

Figure 16: Material velocity wave profiles for shots 2S-593, 69ts-12-09, and 69ts-12-23. Simulated input wave entering the powder is shown by dashed line. Propagated waves (simulated and experimental) shown by solid lines, and are marked with respect to the definitions for α_1, α_2, and α_3 where observable differences exist. Note shock rise time not visible for experimental wave profile on 69ts-12-23.

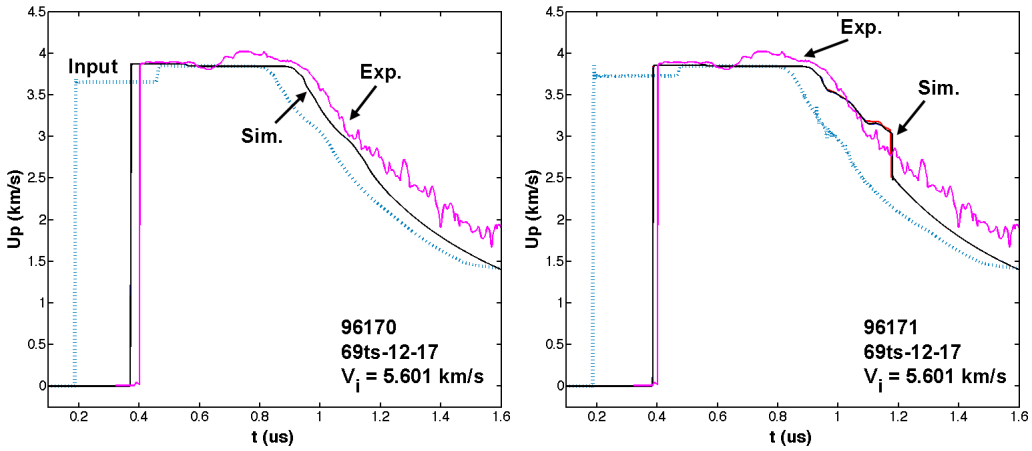

Figure 17: Material velocity wave profiles for shot 69ts-12-17. Simulated input wave entering the powder is shown by dashed line. Propagated waves (simulated and experimental) shown by solid lines, and are marked with respect to the definitions for α_1, α_2, and α_3 where observable differences exist.

powder may also play a role in the observed variation between calculation and experiment. Recalling that the one-dimensional simulations do not explicitly model the SS cell, the simulated increase in material velocity, and corresponding experimentally observed plateau followed by a reduction in material velocity is likely influenced by edge wave effects occurring in the experiment that are not captured by the model. Higher dimensional simulations are required to determine with certainty the origin of this late time difference.

Examination of wave profiles for the next highest impact velocity experiment/simulation, $V_I = 0.405$ km/s, 56-11-27, lends further support to the hypothesis that the sound speed at pressure may be over predicted by calculations in the crush region. In the experimental profiles for this shot the propagated wave gradually approaches its peak state before reaching a quasi-equilibrium state and releasing. In the simulated profiles the shock reaches the same peak state, but upon reaching this state is instantaneously released. Furthermore, in each of the next two higher impact velocity calculations, shots 56-11-55 and 1S-1523, the simulated wave profiles release at a faster rate than that which is observed experimentally. Taken together, these findings suggests that the sound speed at pressure in the compaction regime assigned by both the solid-liquid and three-phase equations of state is higher than the experimental value.

The low impact velocity calculations also highlight the difficulties associated with modeling the viscoelastic and plastic response of the PMMA windows within the current model framework. Some of the earliest shock experiments on PMMA using optical velocimetry to measure wave profiles showed a characteristic gradual rounding near the peak velocity state.[27, 28] A similar rounding is also observed in the propagated wave profiles measured experimentally in shots 56-11-26, -27, and -55, see Fig. 14. However, how much of this characteristic rounding is due to the PMMA, and how much is due to structure imposed by the wave propagating through the porous CeO_2 can not be determined from the present calculations, which define PMMA using isotropic elastic/plastic solid model elements, see Sec. 4.1. While strain-rate strengthening models exist in the current FLAG model libraries, a model with the sophistication required to correctly capture the complex and non-equilibrium response exhibited by polymeric materials (PMMA) under increasing strain-rates is not available. Recently, a continuum glassy polymer model was developed for PMMA at LANL,[29] and

implementation of this model would significantly improve our ability to decouple the combined effects of structure from the window and the powder recorded in an experiment, thereby allowing for the determination and extraction of powder specific wave structures at low pressures.

With the exception of the two lowest impact velocity shots, where release waves from the back of the impactor at the Al/Cu interface and/or edge waves from the surrounding stainless steel cell may influence the measured wave profiles, all of the chosen combinations of equations of state and P-α compaction models do a reasonably good job at predicting the shock breakout time and peak velocity state of the propagated wave. With regard to release profiles, the agreement is less satisfactory, with the general trend observed that release occurs earlier in time in the simulations than it does experimentally. This is illustrated clearly in the propagated profiles for shots 56-11-55 and 1S-1523, where the simulated release profiles occur earlier and are more steep than the experimental profiles. Differences in the experimental setup for the 2S- series of experiments, which included a smaller powder diameter and the use of a PMMA cell instead of SS cell, introduced edge effects into the propagated traces shortly after shock breakout and precludes a meaningful comparison of the release portion of the experiment for shot 2S-589. However, with the limited data set available, it does appear that improvements in our ability to model the release portion of porous CeO_2 could be made by modifications to EOS 96170 and 96171.

6.2 EOS Regime

At impact velocities greater than $V_I > 2.0$ km/s difference in the wave profiles are observed as a result employing the solid-liquid EOS 96170 or the three-phase EOS 96171, where these differences may indicate the onset of a phase transition. The clearest, and possibly the most interesting, illustration of these differences is shown in the results calculated for shot 2S-594 in Fig. 15.

In the experimental profile of shot 2S-594 the material velocity shocks up to the peak state before quickly equilibrating to a steady state and releasing at a later time. This behavior is qualitatively reproduced by the solid-liquid EOS 96170, though the calculated arrival time and onset of release occur earlier in time than observed experimentally. In contrast, the three-phase EOS 96171 predicts a stepped wave profile. For this case the calculation predicts a velocity profile that rises sharply to a velocity lower than in the experiment, before increasing slightly over the course of ∼100 ns. Subsequently, the velocity increases sharply again, before entering into a shallow rising plateau that is in excess of the equilibrium experimental state. Evidence of this stepped structure suggests that the experimental conditions present in shot 2S-594 are on the cusp of the equilibrium transition predicted by EOS 96171, as simulated profiles from higher impact velocities do not exhibit this structure.

In general, choice of the three-phase EOS 96171 results in calculated shock velocities and breakout times that are closer to those measured by experiment. This is clearly illustrated in the simulations of shots 2S-594 and 2S-593 in Fig. 15 and 16, where shock breakout and the rise to the peak velocity state predicted by EOS 96171 nearly overlap with those measured in experiment. Corresponding wave profiles predicted by EOS 96170 arrive early in both instances. With the onset of the equilibrium phase transition observed in the calculated response for shot 2S-594 using the three-phase EOS, the early time shock breakout observed in the simulated profiles of the solid-liquid EOS in these experiments further supports the hypothesis that CeO_2 undergoes (at least a partial) phase transition from cubic fluorite to orthorhombic under shock loading at pressures near 24 GPa. However, as the magnitude of the shock increases to $P > 52$ GPa, breakout predicted with the three-phase EOS begins to arrive noticeably early in time with respect to experiment, see Figs. 16 and 17 and Fig. 12(d). The increasing disagreement between the measured and calculated shock velocities with increasing shock magnitude may indicate that the three-phase EOS 96171 is not calibrated well at high pressures (recall isotherm was only calibrated up to ∼70 GPa), or it may indicate the presence of an additional transition as a result of intense shock heating at elevated pressures. A possible mechanism

of transition may be the CeO_2 to Ce_2O_3 transition, or some other intermediate phase. However, in-situ dynamic x-ray diffraction or Raman scattering experiments are needed to determine if a transition in addition to the cubic to orthorhombic structural transition occurs.

Another interesting feature of the wave profiles for the three highest impact velocity shots that is observed experimentally, but not computationally, is the late time rise in material velocity at the peak state. In shots 69ts-12-09, -23, and -17 this occurs at ∼0.9, ∼0.8, and ∼0.7 μs, respectively, see Figs. 16 and 17. In each of these experiments the material velocity shocks up to its peak equilibrium state and then after some time ramps up to a higher velocity before undergoing release. This behavior is not observed in either the solid-liquid or three-phase EOS simulated profiles. This late time wave structure may be a result of the one-dimensional model not capturing edge effects from the stainless steel cylinder (see Fig. 4). Here, two-dimensional simulations would be of great benefit for determining if this is indeed the case. However, as touched on earlier in Sec. 5.2.2 in an attempt to explain the deviation from U_S-u_P linearity, these experiments could possibly be undergoing a transition outside of the structural cubic fluorite to orthorhombic phase transition. If so, this late time ramp in material velocity may be a manifestation of this transition, though this assertion is at present only speculative.

The late time ramp also appears to have an influence on the release behavior. For shots 69ts-12-09 and -23 the experimentally measured ramp is followed by a sharp release with an inflection at some later that transitions into a more shallow release, see Fig. 16. Of note is that a quasi-kink-like structure is also observed in the release portion of the wave profiles from the three-phase EOS 96171, though this kink is followed by a sharp drop in material velocity as indicated by the arrow in the simulated profile of shot 69ts-12-23 in Fig. 17. Again, the stark differences in the release portion of the wave profiles between the experiment and those predicted by the three-phase EOS indicate the need to perform two-dimensional calculations to determine if this behavior is cell geometry dependent or is indicative of additional physics occurring at the highest pressures investigated.

7 Morphology and Transition

In non-phase transitioning metallic materials like copper, differences in particle size have been shown to have little influence the shock compaction and high-pressure Hugoniot response.[30] While similar conclusions may be drawn from the current data set for CeO_2 in the compaction regime, the same may not be true at elevated pressures where phase transitions may play a more important role in the bulk response. Up to this point, there has been minimal discussion of particle morphologies due to the fact that the continuum simulations performed on CeO_2 do not contain any morphology-specific information. However, at this juncture the calculated and experimentally measured Hugoniot points and wave profiles are examined to determine if there is a morphology-specific influence on the high-pressure behavior.

Inspection of the experimental results given in Table 1 reveals that three different morphology CeO_2 powders were investigated, which were termed the 300 nm, equiax, and rods. Figure 18 shows the morphologies of these powders in the as-received condition, and after pressing the powders to the initial density of $\rho_{00} = 4.03$ g/cm^3, corresponding to the initial condition of the shock experiments. These micrographs illustrate that particle morphologies remain relatively unchanged after pressing for the 300 nm and equiax powders, where all powders are <1 μm in diameter. In contrast, the rods are much larger in the as-received condition, and the initial elongated structure becomes increasingly more blocky and faceted with pressing. Further discussion of particle microstructures in this section refer to those corresponding to the microstructures after pressing, Fig. 18(a-2), (b-2), and (c-2).

The relatively low-pressure dynamic compaction results in Figs. 11 and 12 show that, where similar impact conditions exist between the three morphologies (V_I ∼0.40, ∼0.69 and ∼0.77 km/s), very little difference in the measured Hugoniot response is observed as a result of initial particle morphology. However,

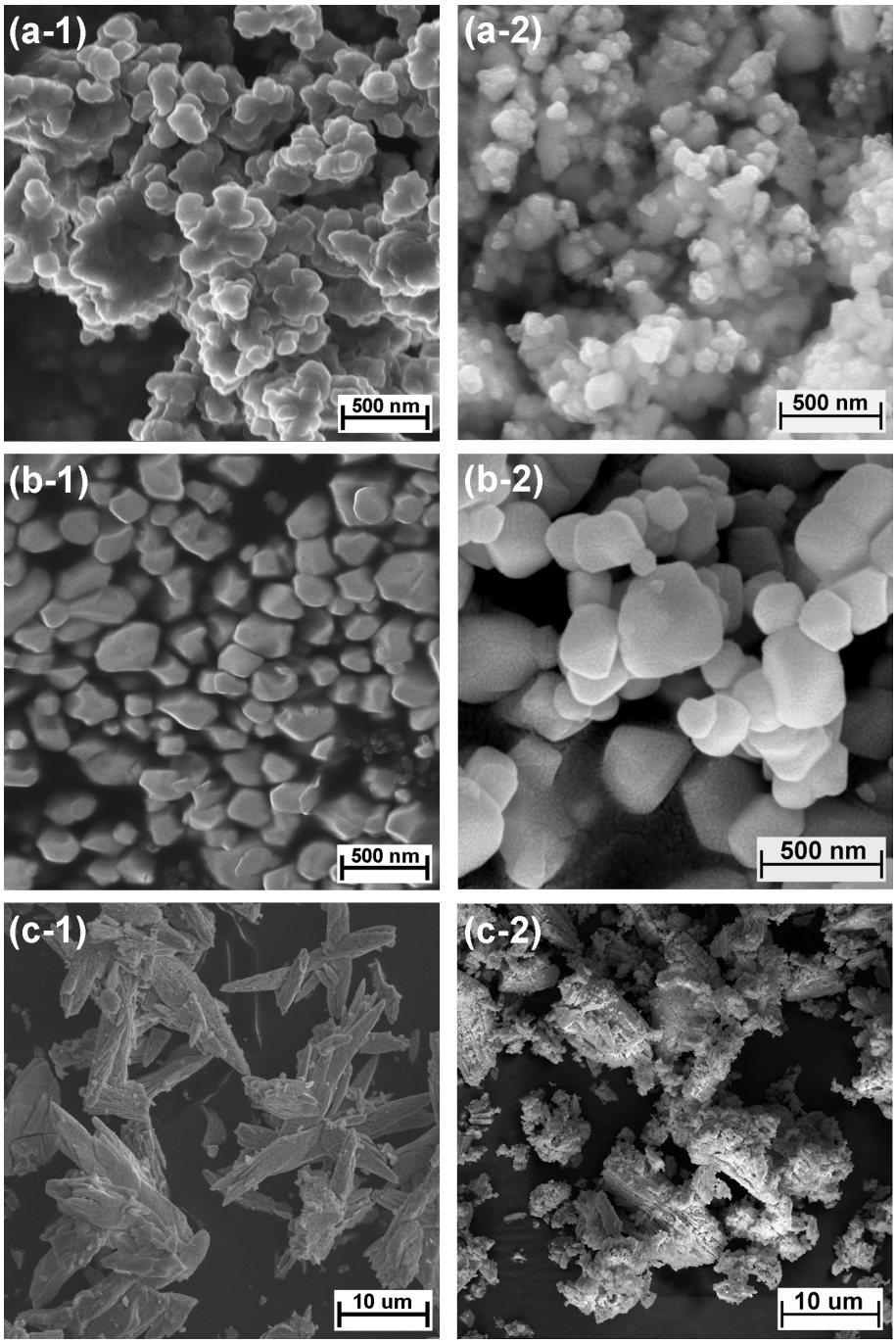

Figure 18: Micrographs of the three CeO_2 powders illustrating morphologies of the as-received (a-1) 300 nm, (b-1) equiax, and (c-1) rods. Micrographs marked with (-2) are representative powder morphologies after the as-received materials were pressed to the initial condition for the shock experiments of $\rho_{00} = 4.03$ g/cm^3.

outside of the compaction regime there is only one impact condition where two distinct morphologies were tested, V_I ~2.3 km/s. Under this shock loading condition both the equiax morphology (2S-648) and the rod morphology (2S-594) CeO_2 powders were tested, see Fig. 19. While the uncertainty limits on experiments 2S-594 and 2S-648 do overlap, the fact that this overlap occurs on either side of the low-pressure solid phase (96170) in P-V space suggests the possibility that the threshold conditions at which the initially cubic fluorite structure CeO_2 transitions to the high-pressure orthorhombic phase may be dependent on initial particle morphology. Note that the rod morphology does not cross the low-pressure solid phase line until reaching a pressure of ~52 GPa, see Fig. 19 shot 69ts-12-09.

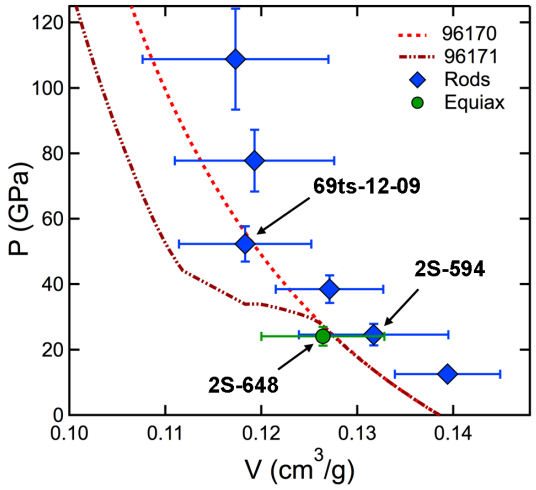

Figure 19: Hugoniot results for equiax and rod morphology CeO_2 powders depicting role of particle morphology on compression and possible phase transition response.

The initial equiax and rod morphologies shown in Fig. 18(b-2) and (c-2) are very different in size, shape, and texture. The equiax particles are small (<1 μm) with smooth blocky surfaces and aspect ratios near unity. In contrast, the rods are much larger (~10 μm) with rough faceted surfaces and the majority of particles having aspect ratios greater than unity. With respect to morphological features and their effect on the shock compression of powders, particle size has been studied the most extensively, and it has been suggested that during shock compaction much of the shock energy is deposited locally at the particle surfaces and contact points.[31] Particle-level simulations support this hypothesis, and calculated temperatures near the particle surfaces can be orders of magnitude higher than in the bulk (interior) of the particle.[32]

What this means for the equiax and rod morphology powders is that depending on particle size, the shock energy could be distributed differently. For the equiax CeO_2 the particle size is small, and energy deposited on the surface due to collisions with neighboring particles can quickly travel to the interior such that the entire particle reaches a quasi-equilibrium state. For the rods, which are an order of magnitude greater in size, the energy deposited on the particle surfaces must travel further to reach the interior, and obtaining a quasi-equilibrium state is expected to take significantly longer than it does for the equiax particles. Examining the calculated P-V Hugoniot results from the three-phase EOS 96171 in Fig. 12(b), it is evident that the response calculated by 96171 lies more closely to the experimental results for the equiax morphology, 2S-648. This suggests that the equiax particles may have reached equilibrium within the temporal duration of the shock front, while the rods have not. If this is true the question naturally arises, when is equilibrium reached during the duration of the shock in the rods? It may be that this does not occur until ~ 52 GPa with shot 69ts-12-09, as this is the point at which the rods cross the low-pressure solid Hugoniot. If this type of size-dependent behavior does indeed occur, then it means that the high-pressure EOS response of CeO_2 may have to be modeled with some type of morphology dependent transition parameter. However, due to the fact that only a single coincident impact condition exists for the two morphology powders, the previous hypotheses regarding a morphology-dependent onset of phase transition must be investigated further. Additional experiments on the equiax material at higher pressures are needed to further examine the role of morphology on the onset of phase transition in CeO_2.

8 Conclusions

This work examined the robustness of SESAME equations of state (EOS) 96170, a solid-liquid EOS for CeO_2 capturing the low-pressure solid cubic fluorite and liquid phases, and EOS 96171, a three-phase CeO_2 EOS which captures both the low-pressure cubic fluorite and high-pressure orthorhombic solid phases as well as the liquid phase. Each of these EOS were combined with a two-term exponential form of the P-α model, where $\alpha(P)$ was determined using three increasingly sophisticated definitions based on the ambient crystal density, α_1, the solid Hugoniot, α_2, and the porous Hugoniot, α_3. Calculations were performed in one-dimension for comparison with experimental shock Hugoniot and velocimetry data, with effects of mesh size, artificial viscosity, and "impedance matching" on the calculated results examined explicitly.

Calculations performed with both the solid-liquid EOS 96170 and the three-phase EOS 96171 were nearly indistinguishable from one another in the low-pressure compaction regime (<5 GPa). Both showed good agreement with experiment for all definitions of $\alpha(P)$, indicating that the chosen form of $\alpha(P)$ had little effect on calculations in this regime. As pressures approached those required to fully solidify the material (∼12 GPa) the chosen definition for $\alpha(P)$ had a greater influence on the calculated response, with predictions based on the solid Hugoniot, α_2, falling outside of the measured experimental uncertainties of U_S and ρ for both EOS 96170 and 96171. However, both the solid-liquid and three-phase EOS nominally predicted the same response at low pressures, which when compared with experimental data suggests that CeO_2 remains in its low-pressure solid phase throughout compaction.

At higher pressures (>24 GPa) calculations performed with the solid-liquid and three-phase EOS began to deviate substantially, suggesting the onset of phase transition in the porous material occurs at or near this threshold pressure. The low-pressure solid EOS shows convergence for the three definitions of $\alpha(P)$ in this range, and all calculations predict a much stiffer and nearly vertical P-V response beginning at 24 GPa. Furthermore, large deviations are observed between the calculated and experimental Hugoniot volumes at high pressures with the solid-liquid EOS. Implementation of the three-phase EOS also shows a nearly linear P-V response beginning at 24 GPa, though predictions are more coincident with experimental results over the entire pressure range. Furthermore, significant deviations in the calculated volumes are observed at high pressures as a result of varying the definitions for $\alpha(P)$ with EOS 96171, where the calculated volume based on α_3 shows the best agreement at the highest pressures.

Calculated and experimental velocimetry profiles were also examined, and it was found that varying the definition for $\alpha(P)$ had a minimal effect on the propagated wave profiles for impact velocities above 0.4 km/s. Results also indicated that the low-pressure Hugoniot data were likely influenced by release and edge wave effects prior to passage of the initial shock for experiments performed at impact velocities below 0.4 km/s, negating a true "Hugoniot analysis" for these experiments. At higher pressures (>52 GPa) an increase in the peak velocity state is observed in the experimental wave profiles, and suggests the possibility of late-time kinetic effects associated with a shock-assisted transformation. This observation promotes the need for performing corresponding two-dimensional simulations under these experimental configurations. Propagated wave profiles coupled with the Hugoniot results also indicate that the onset of phase transition observed in CeO_2 may be influenced by initial particle morphology, though more experimental data is needed to support this hypothesis.

The findings of this report show that the shock response of initially porous CeO_2 exhibits complex behavior at high pressures that cannot be accurately captured by a solid-liquid equation of state. Whether all of the volume compression measured experimentally can be adequately described by the single transition from the cubic to orthorhombic phase remains to be seen. Disagreement between the experimental and three-phase EOS Hugoniot data at the highest pressures, coupled with the variation in onset of linearity in P-V suggests the possibility that additional physics may be active at the highest pressures. It is expected that further refinement to the high-pressure

EOS in addition to performing two-dimensional calculations and additional experiments to capture in-situ phase and/or stoichiometric information would aid significantly in refining our understanding of this material at high pressures.

9 Acknowledgements

Los Alamos National Laboratory is an affirmative action/equal opportunity employer operated by Los Alamos National Security, LLC, for the National Nuclear Security Administration of the U.S. Department of Energy under contract DE-AC52-06NA25396.

References

[1] D.A. Fredenburg, D.D. Koller, *Interpreting the shock response of porous oxide systems*, in Shock Compression of Condensed Matter-2013, Seattle, WA, *in press.*

[2] D.A. Fredenburg, D.D. Koller, P.A. Rigg, R.J. Scharff, J. Appl. Phys. **84** (2013) 013903.

[3] E.D. Chisolm, *SESAME 96170, a solid-liquid equation of state for* CeO_2, LANL Report No. LA-UR-12-21066 (2012).

[4] E.D. Chisolm, *SESAME 96171, a three-phase equation of state for* CeO_2, LANL Report No. LA-UR-12-25524 (2012).

[5] T.J. Vogler, S. Root, M.D. Knudson, W.D. Reinhart, *High-pressure shock behavior of WC and* Ta_2O_5 *powders*, Sandia Report No. SAND2011-6770 (2011).

[6] J.D. Johnson, High Press. Res. **6** (1991) 277.

[7] G.I. Kerley, *User's manual for PANDA: a computer code for calculating equations of state*, LANL Report No. LA-8833-M (1981).

[8] P. Vinet, J.H. Rose, J. Ferrante, J.R. Smith, J. Phys. Condens. Matter **1** (1989) 1941-1963.

[9] S.J. Duclos, Y.K. Vohra, A.R. Ruoff, A. Jayaraman, G.P. Espinosa, Phys. Rev. B **38** (1988) 7755.

[10] L.H. Thomas, J. Chem. Phys. **22** (1954) 1758.

[11] E. Chisolm, S. Crockett, D. Wallace, J. Wills, *Estimating the accuracy of the TFD cold curve*, LANL Report No. LA-UR-03-7346 (2003).

[12] Y.B. Zel'dovich, Y.P. Raizer, *Physics of Shock Waves and High-Temperature Hydrodynamic Phenomena* (Dover Publications, New York 2002) p. 696.

[13] J. Abdallah, *User's manual for GRIZZLY*, Appendix B, LANL Report No. LA-10244-M (1984).

[14] E. Chisolm, C. Greef, D. George, *Constructing explicit multiphase equations of state with OpenSesame*, LANL Report No. LA-UR-05-9413 (2005).

[15] W. Herrmann, J. Appl. Phys. **40** (1969) 2490-2499.

[16] M. Carroll, A.C. Holt, J. Appl. Phys. **43** (1972) 759-761.

[17] D.A. Fredenburg, N.N. Thadhani, J. Appl. Phys. **113** (2013) 043507.

[18] C. Dai, D. Eakins, N. Thadhani, J. Appl. Phys. **103** (2008) 093503.

[19] D.D. Koller, in *Proceedings of the SEM Annual Conference and Exposition of Experimental and Applied Mechanics - 2009* (Curran Associates Inc., New York 2009), Vol. 2, pp. 862-868.

[20] D.E. Burton, *FLAG, Multidimensional Hydrodynamics using Polyhedral Grids*, LANL Report No. LA-UR-97-1109 (1997).

[21] D.J. Benson, Wave Motion **21** (1995) 85-99.

[22] D.L. Preston, D.L. Tonks, D.C. Wallace, J. Appl. Phys. **93** (2003) 211-220.

[23] S.-R. Chen, G.T. Gray III, *Summary of the PTW model parameters* LANL Report No. LA-CP-04–0920 (2004).

[24] Z. Rosenberg, M. Mayseless, G. Rosenberg, in *Shock Compression of Condensed Matter - 1983*, Eds. J.R. Asay, R.A. Graham, G.K. Straub (Elsevier Science Publishers, Amsterdam 1984) pp. 247-249.

[25] M.A. Meyers, *Dynamic Behavior of Materials* (John Wiley and Sons, Inc., New York 1994) p. 186.

[26] O.T. Strand, D.R. Goosman, C. Martinez, T.L. Whitworth, Rev. Sci. Instrum. **77** (2006) 083108.

[27] L.M. Barker, R.E. Hollenbach, J. Appl. Phys. **41** (1970) 4208-4226.

[28] L.M. Barker, R.E. Hollenbach, J. Appl. Phys. **43** (1972) 4669-4675.

[29] B.E. Clements, J. Appl. Phys. **112** (2012) 083511.

[30] R.R. Boade, J. Appl. Phys. **41** (1970) 4542-4551.

[31] W.H. Gourdin, Prog. Mater. Sci. **30** (1986) 39-80.

[32] R.L. Williamson, J. Appl. Phys. **68** (1990) 1287-1296.